

<https://helda.helsinki.fi>

Retrievals of Riming and Snow Density From Vertically Pointing Doppler Radars

Mason, S. L.

2018-12-27

Mason , S L , Chiu , C J , Hogan , R J , Moisseev , D & Kneifel , S 2018 , ' Retrievals of Riming and Snow Density From Vertically Pointing Doppler Radars ' , Journal of Geophysical Research : Atmospheres , vol. 123 , no. 24 , pp. 13807-13834 . <https://doi.org/10.1029/2018JD028603>

<http://hdl.handle.net/10138/307138>

<https://doi.org/10.1029/2018JD028603>

unspecified

acceptedVersion

Downloaded from Helda, University of Helsinki institutional repository.

This is an electronic reprint of the original article.

This reprint may differ from the original in pagination and typographic detail.

Please cite the original version.



Retrievals of riming and snow density from vertically-pointing Doppler radars

S. L. Mason^{1,2}, C. J. Chiu³, R. J. Hogan^{1,4}, D. Moisseev^{5,6}, S. Kneifel⁷

¹Department of Meteorology, University of Reading, Reading, UK

²National Centre for Earth Observation (NCEO), University of Reading, Reading, UK

³Colorado State University, Fort Collins, Colorado, USA

⁴European Centre for Medium-range Weather Forecasts (ECMWF), Reading, UK

⁵Institute for Atmospheric and Earth System Research/Physics, Faculty of Science, University of Helsinki, Finland

⁶Finnish Meteorological Institute, Helsinki, Finland

⁷Institute of Geophysics and Meteorology, University of Cologne, Cologne, Germany

Key Points:

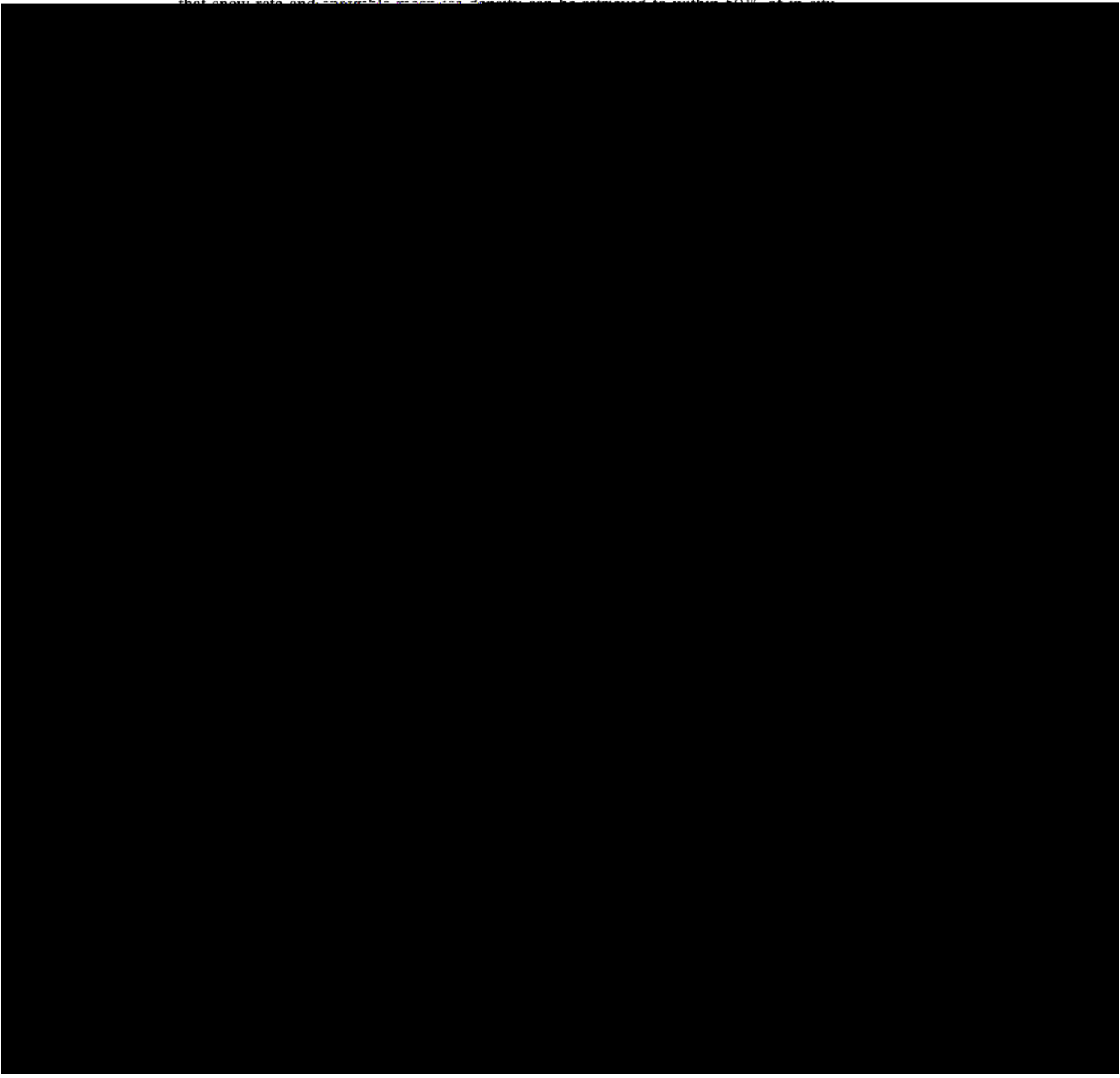
- The CAPTIVATE optimal estimation retrieval algorithm is applied to zenith-pointing Doppler cloud radars deployed during the Biogenic Aerosols—Effects on Clouds and Climate field campaign (BAECC 2014), in Hyytiälä, Finland.
- Doppler velocity is exploited to retrieve a parameter that modulates the mass, area and radar backscatter cross-sections to represent the continuum of particle morphologies from unrimed aggregates to graupel and hail.
- The retrieval provides insights into microphysical processes including aggregation and riming. Retrieved particle density is correlated with the availability of supercooled liquid water, demonstrating potential to use the retrieval to diagnose embedded layers of mixed-phase clouds.

Corresponding author: S. L. Mason, s.l.mason@reading.ac.uk

Confidential manuscript submitted to *JGR-Atmospheres*

22 **Abstract**

23 Retrievals of ice and snow are made from Ka- and W-band zenith-pointing Doppler radars
24 at Hyttiälä, Finland, during the snow experiment (SNEX) component of the Biogenic
25 Aerosols: Effects on Clouds and Climate (BAECC 2014) field campaign. In a novel op-
26 timal estimation retrieval, mean Doppler velocity is exploited to retrieve a “density fac-
27 tor” parameter which modulates the mass, shape, terminal velocity and backscatter cross-
28 sections of ice particles. In a case study including aggregate snow and graupel we find
that snow rate and average mass ice density can be retrieved to within 50% of in situ



169 *Lerber et al.*, 2017]. While integrated quantities such as snow rate are especially sensitive
 170 to the formulation of the mass-size relation [*Heymsfield et al.*, 2010; *Delanoë et al.*, 2014],
 171 in this study it will also be important to relate the mass and shape of particles to their ter-
 172 minal velocity in order to retrieve the morphology of snow particles from Doppler radar
 173 measurements.

174 In the following sections we first describe the PSD (Section 2.2.1), then the mass-
 175 size (Section 2.2.2) and area-size (Section 2.2.3) relations for a range of ice particles,
 176 and finally how particle properties are combined to estimate terminal fallspeeds (Sec-
 177 tion 2.2.4).

178 **2.2.1 Particle size distribution**

179 The PSD is represented as a normalized spectrum of the form

$$N(D) = N_w F(D/D_0). \quad (5)$$

180 where N_w is the normalized number concentration, D_0 is the median volume diameter
 181 [*Testud et al.*, 2001], and the function $F(D/D_0)$ can be either that of the normalized gamma
 182 distribution [*Testud et al.*, 2001; *Illingworth and Blackman*, 2002; *Delanoë et al.*, 2005], or
 183 the universal modified gamma distribution derived by *Field et al.* [2005] for extratropical
 184 ice clouds [see also *Field et al.*, 2007; *Delanoë and Hogan*, 2008]. The normalized number
 185 concentration can be estimated from the moments of the PSD:

$$N_w = M_2^4 / M_3^3 \quad (6)$$

186 where M_n is the n^{th} moment. When using the gamma function a constant shape parame-
 187 ter of $\mu = 2$ is assumed in order to simplify the representation of the PSD; the shape pa-
 188 rameter makes the smallest contribution to uncertainties in the retrieved ice water content
 189 [*Delanoë et al.*, 2005]. In practice for the present study, the differences between the re-
 190 trieved quantities using the normalized gamma and *Field et al.* [2005] PSD were found
 191 to be within the uncertainty of the retrievals; in the results presented here the *Field et al.*
 192 [2005] PSD is used unless otherwise stated.

193 **2.2.2 Mass-size relations**

194 Ice particle mass is expressed as a function of maximum dimension by the power
195 law

$$m(D) = a_m D^{b_m}, \quad (7)$$

196 where the prefactor a_m scales the density of ice at all sizes, and the exponent b_m controls
197 the size-dependence of particle mass and is related to the particle growth mechanism or
198 shape of the particle. Aggregate snowflakes have exponents around $b_m = 2$, close to the
199 theoretical value for fractals [Westbrook *et al.*, 2004; Stein *et al.*, 2015]. More rounded
200 graupel and hail particles have exponents closer to $b_m = 3$, the physical maximum for
201 spheres [Leinonen and Moisseev, 2015].

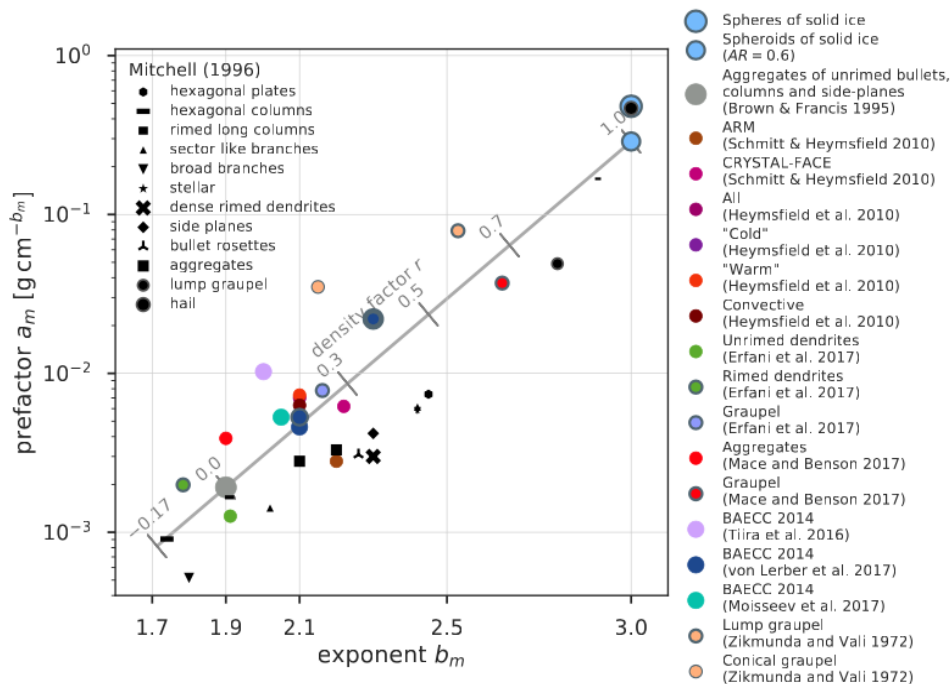
202 While snow particles are observed to vary greatly in morphology, the majority of
203 snow is thought to fall as aggregate snowflakes [Langleben, 1954]—indeed, the mass-size
204 relations used for ice and snow tend to be derived from measurements dominated by un-
205 rimed aggregates. We follow the approach of Hogan *et al.* [2012], who showed that in-
206 situ measurements of cirrus were consistent with radar reflectivities when the mass-size
207 relation derived for “aggregates of unrimed bullets, columns and side-planes” by Brown
208 and Francis [1995] was used. In this representation the smallest particles are assumed
209 to be solid quasi-spheroidal ice crystals, while larger aggregates occupy the volume of a
210 horizontally-aligned oblate spheroid with an aspect ratio—that between the minimum (ver-
211 tical) dimension and the maximum (horizontal) dimension—of $AR = 0.6$. Hogan *et al.*
212 [2012] found that this value provided a good fit to a database of aircraft measurements
213 as well as other studies in the literature. Combining dual-polarization weather radar and
214 surface based snowfall measurements at Hyytiälä, [Li *et al.*, 2018] found that the aspect
215 ratio varies with riming fraction between 0.4 and 0.9, while analysis of PIP images by
216 Tiira *et al.* [2016] yielded a median aspect ratio of 0.72. However, the applicability of
217 particle images to derive particle geometrical properties was questioned by Jiang *et al.*
218 [2017]; hence, Tiira *et al.* [2016] also used a single aspect ratio value of 0.6 for density
219 retrievals. In the present study it was found that assuming $AR = 0.8$ instead of $AR = 0.6$
220 led to an increase in retrieved ice water content of approximately 20%, demonstrating that
221 the shape and orientation of ice particles is an important uncertainty in the remote-sensing
222 of snow [see also Hogan and Westbrook, 2014].

223 How does riming affect the mass-size relation of snow? Numerical analogues for
224 “ballistic” collisions between ice particles (aggregation) and between ice particles and su-
225 percooled liquid drops (riming) suggest that aggregating particles will retain mass-size
226 exponents around $b_m = 2$, while those growing by riming will tend toward exponents of
227 $b_m = 3$ [Jullien, 1992]. A conceptual model for riming introduced by Heymsfield [1982]
228 proposes a two stage process for the riming of aggregate snowflakes [see also Morrison
229 and Milbrandt, 2015; Moisseev et al., 2017], in which an aggregate is first “filled in” by
230 freezing supercooled drops, increasing the mass of the particle but not its size: this in-
231 creases the prefactor of the mass-size relation while the exponent remains close to $b_m = 2$
232 [e.g. Szyrmer and Zawadzki, 2014a; Morrison and Milbrandt, 2015; Moisseev et al., 2017;
233 von Lerber et al., 2017]. That the first stage of riming does not scale the exponent of the
234 mass-size relation is consistent with earlier studies of rimed snow [e.g. Harimaya and
235 Sato, 1989; Mitchell et al., 1990]. Once the particle geometry is closed by in-filling, it
236 is classified as graupel. In this second stage rime is accreted to the outside of the particle,
237 adding to both its mass and diameter, and as the particles become rounder in shape the
238 exponent approaches $b_m = 3$ [Mitchell, 1996]. The morphology of an ice particle encodes
239 a history of multiple and interacting processes, including aggregation and transitions be-
240 tween stages of riming, which may be observed microscopically [Fujiyoshi and Wakahama,
241 1985] or tracked within a microphysical parameterization scheme [Morrison et al., 2015;
242 Morrison and Milbrandt, 2015], but are unlikely to be instantaneously grasped by remote
243 sensing. In a modelling study Leinonen and Szyrmer [2015] compared particles that have
244 grown first by aggregation then riming to those that have grown by simultaneous aggrega-
245 tion and riming. While it was found that aggregation and riming, whether in series or in
246 parallel, form particles that are indistinguishable in terms of radar backscatter—an impor-
247 tant result for remote-sensing—the corresponding mass-size relations were distinct: when
248 riming followed aggregation the exponent was found to remain close to $b_m = 2.1$ until a
249 relatively high degree of riming; but when riming and aggregation were simultaneous the
250 exponent varied significantly even at low degrees of riming. This complicates the two-
251 stage conceptual model of riming. While we may attempt to formulate a representation of
252 the range of morphologies and densities of ice particles for remote-sensing applications,
253 the possibility of multiple interacting ice processes means we should be cautious about
254 attributing all variations in particle density to riming.

255 It has been observed that the mass-size relations derived from studies of snow and
 256 ice form a continuum of ice particles from unrimed snowflakes to graupel and hail [*Lin*
 257 *and Colle, 2011*]; Fig. 1 shows the mass-size prefactors and exponents a_m and b_m in cgs
 258 units and converted where necessary into terms of maximum particle dimension D . Parti-
 259 cles with low mass-size prefactors and exponents—in the lower left part of the diagram—
 260 include a range of unrimed aggregates, as well as other low-density species such as den-
 261 drites, needles and columns. Measurements of unrimed snow from ground-based studies
 262 [*Tiira et al., 2016; von Lerber et al., 2017*] are consistent with aircraft studies of ice clouds
 263 [*Heymsfield and Westbrook, 2010; Brown and Francis, 1995*], with b_m varying between
 264 1.9 and 2.1. Larger mass-size prefactors and exponents—in the centre to the upper-right
 265 part of the diagram—include denser or more compact particles of various kinds, often
 266 with some degree of riming. Exponents for rimed aggregates and low-density graupel are
 267 between 2.1 and 2.4 [*Erfani and Mitchell, 2017; von Lerber et al., 2017*]; while for lump
 268 graupel and hail classifications [*Mitchell, 1996; Mace and Benson, 2017; Zikmunda and*
 269 *Vali, 1972*] the exponent approaches 3.0. We note that the position on the mass-size re-
 270 lation diagram is not solely related to the effect of riming, especially for slender 1- and
 271 2-dimensional species such as columns and dendrites: for example, the rimed dendrites in
 272 *Erfani and Mitchell [2017]* have a lower mass-size exponent than the unrimed dendrites;
 273 and the different sizes of hexagonal columns in *Mitchell [1996]* range from the upper-right
 274 part of the diagram for the smallest columns, to the extreme lower-left for the largest.

281 Variations in ice particle density have been parameterized in many ways. Fixed den-
 282 sities can be assumed depending on the cloud type, with low-density aggregates in strat-
 283 iform cloud and graupel-like particles in convective cloud [e.g. *Greco et al., 2016*]. *Lin*
 284 *et al. [2011]* parameterize ice density according to temperature. *Szyrmer and Zawadzki*
 285 *[2014a]* demonstrate a radar retrieval of lightly rimed snow from ground-based dual-frequency
 286 Doppler radars in which the prefactor a_m is scaled to increase the density of ice due to
 287 riming, while the exponent is fixed at $b_m = 2$. Similarly, *Moisseev et al. [2017]* repre-
 288 sented the density of snow by scaling the prefactor of the mass-size relation and holding
 289 the exponent constant.

290 In order to represent a continuum of ice particles from unrimed and rimed aggre-
 291 gates to graupel and hail, we parameterize particle mass based on a “density factor” r
 292 (grey line in Fig. 1) that is continuous between the mass-size relation for the unrimed ag-
 293 gregates of *Brown and Francis [1995]* ($m = 0.0121 D^{1.9}$ kg where $r = 0$) and that of oblate



275 **Figure 1.** A comparison of $m(D)$ power-law prefactors and exponents. Coloured circles show a_m, b_m for
 276 various studies of ice and snow. Black markers correspond to particle types summarized in *Mitchell* [1996];
 277 where multiple markers of a particular type are shown, their relative size indicates the size range for which
 278 the mass-size relation was derived. Unrimed aggregates [*Brown and Francis, 1995*] and spheroids of solid
 279 ice define the mass-size relation as a function of density factor r : the grey line indicates the values of a_m, b_m
 280 parameterized by the density factor in the range $-0.17 < r < 1.0$.

294 spheroids of solid ice ($m = 288 D^3$ kg at $r = 1$). The parameterized exponent varies lin-
 295 early with density factor between these two reference points ($b_m = 1.9$ and $b_m = 3$):

$$b'_m(r) = 3r + 1.9(1 - r), \quad (8)$$

296 while the prefactor is scaled according to the requirement that particle masses are equiva-
 297 lent for all r at some critical diameter D_c , which can be calculated as $(0.0121/288)^{1/(3-1.9)} = 105 \mu\text{m}$,
 298 similar to the transition from quasi-spheroids to aggregates in *Hogan et al.* [2012]. Nor-
 299 malizing by the critical diameter, the mass-size relation for all particles can be expressed

$$m(D, r) = a'_m \left(\frac{D}{D_c} \right)^{b'_m}, \quad (9)$$

300 where the normalized prefactor $a'_m = a_m D_c^{b_m} = 33.3 \mu\text{g}$ is the particle mass at the critical
 301 diameter. A similar normalized mass-size relation was employed in *Szyrmer and Zawadzki*
 302 [2014a] [see also *Maahn et al.*, 2015; *Maahn and Löhnert*, 2017], but in that study the
 303 critical diameter was selected to be close to the median particle diameter to minimize the
 304 effect of fixing the exponent of the mass-size relation $b_m = 2$. In the present retrieval all
 305 particles smaller than the critical diameter are assumed to be solid quasi-spheroids; ex-
 306 pressed another way, the fractional volume of a particle occupied by ice is given by the
 307 ice fraction,

$$f(D, r) = \begin{cases} 1.0 & D \leq D_c \\ (D/D_c)^{b'_m-3} & D > D_c \end{cases} \quad (10)$$

308 The ice fraction-size relation for a range of density factors is shown in Fig. 3.

309 In terms of the density factor, the unrimed and lightly-rimed snow correspond to
 310 low values ($r < 0.3$), and heavily-rimed snow and graupel [*von Lerber et al.*, 2017; *Mace*
 311 *and Benson*, 2017] relate to higher values ($0.3 < r < 0.7$). While $r = 1$ is the upper limit,
 312 small negative density factors are possible, and allow for the representation of particles
 313 with lower densities such as dendrites [*Erfani and Mitchell*, 2017] or large hexagonal columns
 314 [*Mitchell*, 1996].

315 We note that the density factor is not intended to explicitly represent the effect of
 316 the riming process on the mass of a particle, but allows for a smooth transition between
 317 unrimed and rimed aggregates to graupel and hail which we hope will be sufficient to al-
 318 low an estimate of ice morphology based on particle fallspeeds. The density factor pivots
 319 the mass-size relation of ice particles larger than the critical diameter (Fig. 3), but with-
 320 out representing the transition features that would corresponding to the multiple stages of

321 riming. A more process-oriented parameterisation of the “in-filling” stage of rimed aggregate
 322 snowflakes would be to scale the mass-size prefactor with the density factor, while
 323 the exponent remains constant. While this would better represent the conceptual model of
 324 the riming process, it would not encompass the observed variability in the mass-size relations
 325 of unrimed snowflakes, or the transition to graupel-like particles. A comparison of
 326 the two parameterisations indicated that the retrieval was not strongly sensitive to the representation
 327 of the density factor, especially for estimates of unrimed to moderately rimed
 328 aggregates. With additional observational evidence, a more complex representation of the
 329 effects of riming on particle morphology—including expected changes in the masses and
 330 shapes of particles during different stages of riming—may allow for improved retrievals
 331 and better quantified uncertainties. This should be the subject of future work.

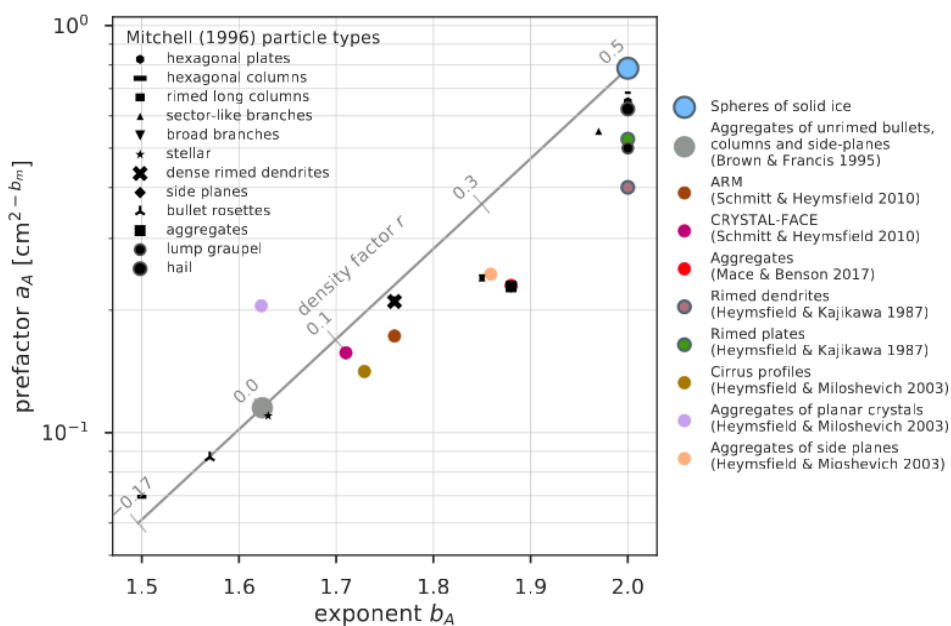
332 **2.2.3 Area-size relation**

333 Similar to the mass-size relation, the cross-sectional area of ice particles is expressed
 334 as a power law:

$$A = a_A D^{b_A}. \quad (11)$$

335 The area-size relation of unrimed aggregates is derived from the mass-size [*Brown and*
 336 *Francis, 1995*] and mass-area relations [*Francis et al., 1998*] from aircraft measurements
 337 of cirrus clouds $A = 0.02038 D^{1.624} \text{ m}^2$ in SI units and in terms of maximum dimension.
 338 The geometric upper limit for horizontally-aligned oblate spheroids with maximum dimension
 339 on the horizontal plane is $A = \pi/4 D^2 \text{ m}^2$. A comparison of area-size relations
 340 from a range of studies (Fig. 2) again shows a relationship between the prefactors and exponents
 341 across particle types: lower density factors are consistent with unrimed ice particles
 342 [*Schmitt and Heymsfield, 2010; Mace and Benson, 2017*], and larger density factors
 343 with rimed particles [*Heymsfield and Kajikawa, 1987*], graupel and hail [*Mitchell, 1996*].
 344 While increases in cross-sectional area are consistent with the conceptual model of riming
 345 leading to the in-filling of aggregates and a transition to rounded graupel-like particles,
 346 there is significant variability between particle types: for example, columns may retain
 347 low cross-sectional areas despite riming, while riming may have little effect on the cross-sectional
 348 area of plates.

354 To represent the increased cross-sectional area of rimed aggregates and graupel, we
 355 scale the area-size relation by the density factor r ; however, to represent the more rounded



349 **Figure 2.** A comparison of power law prefactors and exponents for ice particle area-size relations.
 350 Coloured circles show a_A, b_A derived from a range of aircraft and surface studies. Black markers corre-
 351 spond to specific particle types summarized in Mitchell [1996]. The parameterized area-size relation, which
 352 varies with density factor between unrimed aggregates [$r = 0$ Brown and Francis, 1995; Francis et al., 1998]
 353 and spheres of solid ice ($r = r_{max}$), is shown with a grey line.

356 shapes of heavily rimed aggregates and graupel, the cross-sectional area is maximized for
357 $r = r_{\max}$, so that

$$b'_A = 2\frac{r}{r_{\max}} + 1.624\left(1 - \frac{r}{r_{\max}}\right). \quad (12)$$

358 The prefactor is scaled by a critical diameter D_{cA} , the size at which the cross-sectional
359 area of unrimed aggregates and spheres are equal, which can be calculated to be $61 \mu\text{m}$.
360 The normalized area-size relation is therefore

$$A = a'_A \left(\frac{D}{D_{cA}}\right)^{b'_A} \quad (13)$$

361 where the modified prefactor is the area at the critical diameter $a'_A = a_A D_{cA}^{b'_A}$. Most rimed
362 and unrimed aggregates correspond to density factors $r < 0.3$, while quasi-spheroidal and
363 heavily rimed particles, graupel and hail have $r \approx r_{\max}$. A marginally more complex area-
364 size relation that better fits the observations would be to allow both the prefactor and ex-
365 ponent to vary for $r < r_{\max}$, before scaling only the prefactor up to $r = 1$.

366 Particle area is often expressed as the area ratio, which is the cross-sectional area of
367 the particle normalized by area of the circumscribing circle, or

$$A_r(D) = \begin{cases} 1.0 & D \leq D_{cA} \\ (D/D_{cA})^{b'_A-2} & D > D_{cA} \end{cases}. \quad (14)$$

368 **2.2.4 Velocity-size relation**

369 The boundary layer or hydrodynamic method provides an estimate of the terminal
370 velocity of a hydrometeor based on size, area ratio and mass [e.g. *Mitchell, 1996; Mitchell*
371 *and Heymsfield, 2005; Khvorostyanov and Curry, 2005; Heymsfield and Westbrook, 2010*]
372 or conversely, an estimate of particle mass from measured diameter, cross-sectional area
373 and fallspeed [e.g. *von Lerber et al., 2017*]. In the previous sections the mass- and area-
374 size relations for ice particles were expressed as functions of diameter and density fac-
375 tor; hence a look-up table for particle terminal velocities is produced using the method of
376 *Heymsfield and Westbrook [2010]*.

381 The terminal fallspeed of ice particles $v(D, f)$ for a range of maximum dimensions
382 and ice fractions (see eq. 10) is overlaid with curves corresponding to the mass-size rela-
383 tions for a range of density factors (Fig. 3). As the mean Doppler velocity relates to the
384 reflectivity-weighted average of particle fallspeeds, the density factor has the greatest effect
385 on the fallspeeds of the largest particles. While the largest unrimed aggregates do not ex-

386 exceed terminal velocities of 2 m s^{-1} , even low density factors effect significant increases in
387 fallspeed for particles of the same size.

388 **2.3 State variables**

389 **2.3.1 Extinction coefficient and primed number concentration**

390 The choice of retrieved state variables is flexible within CAPTIVATE, as are any
391 vertical or temporal smoothing applied to the state variables. In this retrieval, a state vari-
392 able related to the density factor is added to those used for retrievals of ice clouds from
393 radar–lidar synergy described in *Delanoë and Hogan* [2008, 2010]. The first state variable
394 is the visible extinction coefficient of ice in the geometric optics approximation, α_v . The
395 second state variable is the primed number concentration,

$$N'_0 = N_w \alpha_v^{-0.6} \quad (15)$$

396 from which the normalized number concentration N_w from (5) can be recovered, since the
397 extinction coefficient is also retrieved. *Delanoë and Hogan* [2008] showed using in situ
398 aircraft data that this choice of state variables for ice allows for a convenient a priori es-
399 timation of the primed number concentration as a function of atmospheric temperature
400 (Table. 1). An additional parameter, the lidar extinction-to-backscatter ratio, can also be
401 retrieved in radar-lidar synergy applications; however, in this study we assume this vari-
402 able is constant.

403 The minimization scheme does not limit the values of retrieved variables, so we for-
404 mulate state variables such that they remain physically meaningful at all values; this is
405 achieved by using the natural logarithms of N'_0 and α_v .

406 While these choices of state variables for ice and snow are convenient for the rea-
407 sons described above, they are not necessarily the most physically meaningful quantities.
408 For comparison with in situ measurements, an integrated quantity such as the melted-
409 equivalent snow rate, as well as the median diameter and normalized number concentra-
410 tion, are more convenient. As the extinction coefficient is an integral over the PSD and
411 the primed number concentration relates to a parameter of the PSD by (15), the two state
412 variables are sufficient to calculate the PSD.

413 **2.3.2 Density index**

414 The natural logarithm of the density factor is not a suitable state vector; the density
415 factor should not exceed $r = 1$, but small negative values are physically meaningful. In-
416 stead we retrieve the density index r' , a state variable defined such that:

$$r = \frac{f(r' + r_0) + f(r_0)}{1 - f(r_0)}, \quad (16)$$

417 where

$$f(x) = \frac{1}{2} + \frac{\tan^{-1} x}{\pi} \quad (17)$$

418 and $r_0 = -2$. This transform function has the property that $r = 0$ when $r' = 0$, and for any
419 value of r' , r is within the range -0.173 to 1.0 . The transform is illustrated in Fig. 4.

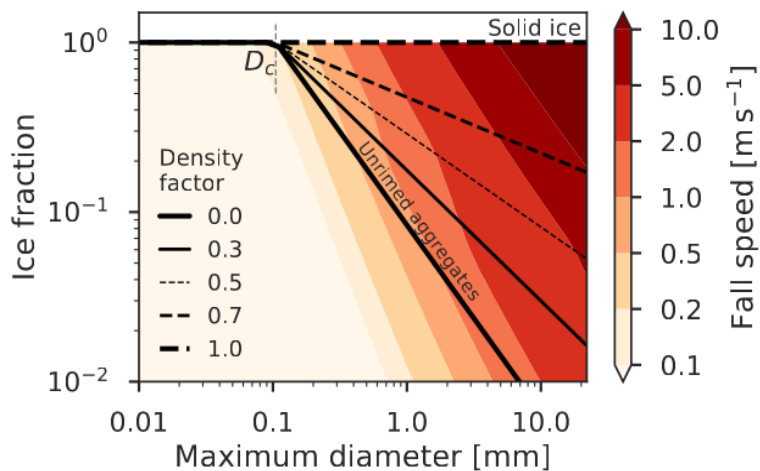
423 **2.3.3 Representation of the state vector**

424 To reduce the effect of measurement noise on the retrieval, the profile of each state
425 variable is represented as the basis functions of a cubic spline [Hogan, 2007]. The degrees
426 of freedom of the retrieval can therefore be controlled by altering the spacing of the basis
427 functions, which modifies the effective scales over which features are retrieved [Rodgers,
428 2000]. A Kalman smoother [Rodgers, 2000] is applied to the extinction coefficient and
429 density index, so that the retrieval of these quantities is constrained by adjacent profiles.
430 In the first pass of the smoother the retrieval is constrained by subsequent rays and, on
431 the second pass, in both directions. For the retrieval of the density factor, this will have
432 the effect of filtering out smaller-scale fluctuations in the mean Doppler velocity due to
433 turbulent vertical air motion.

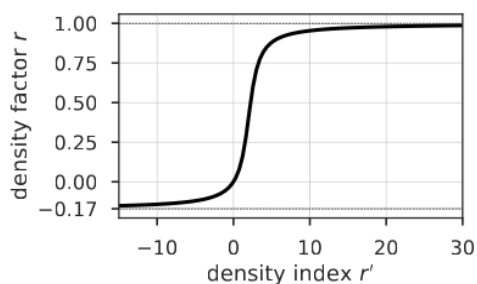
The state vector for ice cloud and snow is therefore

$$\mathbf{x}_{\text{ice}} = \begin{pmatrix} \ln \alpha_v \\ \ln N'_0 \\ r' \end{pmatrix}.$$

434 The prior estimate of the state vector and associated uncertainties represent our knowledge
435 of the state before the measurement vector is assimilated. The values and uncertainties
436 of the priors, and the vertical representation of each state variable are summarized in Ta-
437 ble 1; note that the uncertainties in the priors are in terms of the natural logarithm of the
438 physical parameters. From a large database of in situ measurements of ice clouds [De-
439 lanoë *et al.*, 2005] an expression has been derived for $\ln N'_0$ as a function of atmospheric



377 **Figure 3.** The terminal fallspeeds $v(D, f)$ of ice particles as a function of maximum dimension D , and
 378 ice fraction f . Black lines correspond to the parameterized mass-size relations for density factors between
 379 unrimed aggregates ($r = 0$) and spheroids of solid ice ($r = 1$). D_c is the diameter below which all particles
 380 are represented as dense quasi-spheroidal particles.



420 **Figure 4.** The transform function between density index r' , the retrieved state variable, and the density
 421 factor which modulates the particle properties between unrimed aggregates at $r = 0$ and spheroids of solid ice
 422 at $r = 1$.

446 **Table 1.** State variables for ice and snow, their priors, uncertainties and vertical representation. Note that
 447 we take as the state variables the natural logarithms of key parameters; stated uncertainties are therefore
 448 uncertainties in the natural logarithm of the priors.

State variable \mathbf{x}_i	Prior \mathbf{x}_i^a	Prior uncertainty $\sigma(\mathbf{x}_i^a)$	Cubic spline spacing [m]
Extinction coefficient $\ln \alpha_v$	$-9.2103 - 0.03148 T$ (where T is in $^{\circ}C$)	10.0	150
Primed number concentra- tion $\ln N'_0$	$23.03 - 0.12997 T$ (where T is in $^{\circ}C$)	1.0	600
Density index r'	0.0	1.0	150

440 temperature, with a variance of 1.0 [Fig. 3b in *Delanoë and Hogan, 2008*], and a similar
 441 function of temperature is used for the prior extinction coefficient. When fewer observa-
 442 tional variables are used it may be necessary to reduce the number of degrees of freedom
 443 by holding some state variables at their a priori values; these state variables can be repre-
 444 sented within the retrieval as a “model” variable, wherein its value does not vary but its
 445 prior uncertainty is assimilated.

449 2.4 Observed variables and radar forward model

450 2.4.1 Reflectivity factor

451 The observed variables for each radar are the apparent radar reflectivity factor Z_f
 452 and mean Doppler velocity V_f at the radar frequency f . The reflectivity factor is given by

$$Z_f = 10^{18} \frac{\lambda^4}{\pi^5 |K_f|^2} \int_0^{\infty} \sigma_f(D) N(D) dD \quad (18)$$

453 where λ is the radar wavelength, K_f is the dielectric factor, and $\sigma_f(D)$ is the radar backscat-
 454 ter cross-section. Radar attenuation due to atmospheric gases is modelled from the at-
 455 mospheric state using *Liebe* [1985], so that this effect is included in the observed and
 456 forward-modelled radar reflectivities.

457 Attenuation due to liquid water can be significant for millimetre-wavelength radars,
 458 and can either be accounted for by simultaneously retrieving the liquid water content, or
 459 by correcting for attenuation in the radar reflectivities prior to the retrieval. The former

option is most suited to a radar–lidar–radiometer retrieval wherein the lidar backscatter and a visible radiance may provide adequate constraints; for a radar-only retrieval the available observed variables are dominated by ice, and the retrieval of liquid water content would be underconstrained. Radar reflectivities can be pre-corrected for liquid attenuation based on an estimate of the liquid water path, such as from a microwave radiometer. In this study we follow the correction described in *Kneifel et al.* [2015]; the vertical distribution of SLW not being known, it is distributed evenly over the lowest 4 km of the atmosphere. Alternative corrections may be made by assuming all of the attenuation takes place below the lowest radar gate, or by locating the liquid in one or more shallow layers based on other evidence such as a recent sounding, or Doppler spectra [e.g. *Kalesse et al.*, 2016]. In practice we found that the uncertainty in W-band radar reflectivity between the different corrections was on the order of 1 to 2 dB; this can be accounted for within CAPTIVATE by increasing the observational uncertainty applied to the measurement vector (see Section. 2.4.4).

Reflectivity enhancement due to radar multiple scattering can be modelled using the method of *Hogan* [2008]; however, in this application with ground-based narrow beamwidth radars, we assume multiple scattering is negligible. The uncertainty in the radar reflectivity includes both observational and forward-model errors.

2.4.2 Mean Doppler velocity

Mean Doppler velocity is the reflectivity-weighted fallspeed of hydrometeors

$$V_f = \frac{\int_0^\infty v(D) \sigma_f(D) N(D) dD}{\int_0^\infty \sigma_f(D) N(D) dD}, \quad (19)$$

where $v(D)$ is corrected for air density, and positive values of mean Doppler velocity are toward the surface. The forward-modelled mean Doppler velocity neglects air motion, the effects of which are also included in the observational uncertainty. In the stratiform snow events in this study we assume that the mean Doppler velocity is dominated by the terminal velocities of hydrometeors rather than vertical air motions. In convective situations or where ice particles are very small, this assumption may not be justified, and would lead to a misdiagnosis of particle density; this will be considered in Section 4.1.

487 **2.4.3 Scattering models**

488 In addition to the density and shape of snow particles (Section 2.2), variability in
489 particle morphology has a significant impact on the scattering of microwave radiation,
490 which must be approximated within the radar forward-model. The self-similar Rayleigh-
491 Gans approximation [SSRGA; *Hogan and Westbrook, 2014; Hogan et al., 2017*] provides
492 an accurate estimate of the radar backscatter cross-section for unrimed aggregates, but un-
493 derestimates the radar backscatter of higher-density rimed particles. Snow particles have
494 often been approximated by “soft spheroids”—oblate spheroids composed of a homoge-
495 nous mixture of ice and air—for which the radar backscatter can be estimated using the
496 **T**-matrix method [e.g. *Hogan et al., 2012*]. *Leinonen and Szyrmer* [2015] found that soft
497 spheroids provide a good approximation to the backscatter of dense graupel-like particles,
498 but not to rimed aggregates. In both approximations particles are represented as occupy-
499 ing the volume of horizontally-aligned oblate spheroids with an aspect ratio of $AR = 0.6$
500 [*Hogan et al., 2012*].

501 In the absence of an explicit model for rimed aggregates, we represent the backscat-
502 ter cross-section in the transition from unrimed aggregates to graupel as an external mix-
503 ture between SSRGA ($r \leq 0.2$) and soft spheroids ($r \geq 0.5$). These thresholds were se-
504 lected based on the ranges of density factors associated with mass-size relations for stud-
505 ies of unrimed aggregates and graupel (Fig. 1). As a check on this representation, the
506 forward-modelled radar backscatter from a gamma distribution of particles was used to
507 generate dual-wavelength ratios (DWRs) at Ka–W-bands and X–Ka-bands for a range of
508 density factors (Fig. 5); these curves are overlaid with triple-frequency radar measurements
509 from three snow events during BAecc 2014 [*Kneifel et al., 2015, c.f. their Fig. 1*]. A thin
510 contour highlights the most frequent DWRs observed during the snow event that is stud-
511 ied in Section 4.1. The upright band of $DWR_{Ka-W} < 10$ dB and large DWR_{X-Ka} corre-
512 sponds to the “hook” feature identified for unrimed aggregates, while the flat feature with
513 low DWR_{X-Ka} is associated with denser graupel-like particles. The triple-frequency sig-
514 natures represented by SSRGA ($r \leq 0.2$) resemble those of unrimed aggregates, while the
515 soft spheroids ($r \geq 0.5$) fit the flatter signature associated with graupel. This demonstrates
516 that a simple hybrid representation at least qualitatively permits the signatures of unrimed
517 aggregates and dense rimed particles in multiple-frequency radar observations—but does
518 not necessarily address known limitations in the soft spheroid approximation for a range
519 of dense particles [*Leinonen and Szyrmer, 2015; Hogan et al., 2017*]. The modelling and

520 measurement of the morphology and multiple-frequency radar scattering of ice particles
 521 are of significant research interest [e.g. *Kneifel et al.*, 2018], and improved approximations
 522 for the backscatter cross-sections for rimed aggregates will both reduce uncertainties in the
 523 present retrieval, and allow for increased confidence in multiple-frequency radar retrievals
 524 of snow.

532 **2.4.4 Measurement vector**

The vector of observed variables for a dual-frequency Doppler radar retrieval is

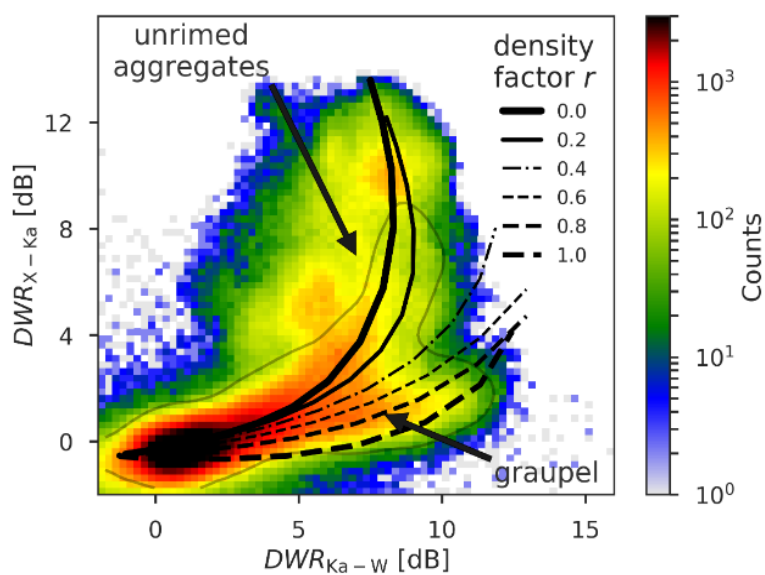
$$\mathbf{y} = \begin{pmatrix} Z_{f_0} \\ V_{f_0} \\ Z_{f_1} \\ V_{f_1} \end{pmatrix}.$$

533 In principal more than two radar frequencies could be included in the measurement vector;
 534 and in practice, as discussed in the next section, some of the observed variables may not
 535 be assimilated in the present study.

536 The uncertainties in the measurement vector includes the stated measurement er-
 537 ror for the instruments (Table 2), other sources of observational uncertainty, and an esti-
 538 mate of the uncertainties in the assumptions that form the basis of the instrument forward-
 539 model. For a retrieval that relies upon the mean Doppler velocity to estimate the proper-
 540 ties of hydrometeors, the treatment of and sensitivity to uncertainties in Doppler measure-
 541 ments are of particular interest. For the present study we assume uncertainties of 3 dB in
 542 the radar reflectivities and 1.0 m s^{-1} in the mean Doppler velocity.

543 **3 BAECC 2014 data**

544 As part of the Biogenic Aerosols—Effects on Clouds and Climate field campaign
 545 [BAECC 2014; *Petäjä et al.*, 2016], the US Department of Energy atmospheric radia-
 546 tion measurement (ARM) program’s second mobile facility (AMF2) was deployed at the
 547 University of Helsinki’s Hyytiälä forestry field station ($61^\circ 51' \text{N}$, $24^\circ 17' \text{E}$). The remote-
 548 sensing and in situ instrumentation, and their deployment are documented in *Kneifel et al.*
 549 [2015]. Between 1 February and 31 March 2014 the snowfall measurement experiment
 550 (SNEX) intensive observation period (IOP) focused on the measurement of snow micro-
 551 physics. Remote-sensing observations include vertically-pointing Doppler radars, lidar and



525 **Figure 5.** Joint histogram of measured dual-wavelength ratios (DWRs) for triple-frequency radar ob-
 526 servations from the three cases studied in *Kneifel et al.* [2015]; a thin contour encloses the most frequent
 527 measurements during the February 21–22 2014 case considered in Section 4.1, highlighting distinct features
 528 associated with aggregates and graupel. Black curves represent the forward-modelled DWR for an expo-
 529 nential distribution of particles with density factors from unrimed aggregates (using SSRGA for $r < 0.2$) to
 530 graupel (“soft spheroids” for $r > 0.5$); the transition between rimed aggregates and graupel is represented by
 531 an external mixture of the two approximations to the radar backscatter cross-section.

566 **Table 2.** AMF2 zenith-pointing radar instruments and observational uncertainties

Instrument	KAZR	MWACR
Frequency	35 GHz	95 GHz
Wavelength	8.6 mm	3.2 mm
Gate spacing	30 m	30 m
Beam width	0.38 °	0.3 °
Reflectivity uncertainty	1 dB	1 dB
Mean Doppler velocity uncertainty	0.5 m s ⁻¹	n/a

562 microwave radiometer instruments, and the state of the atmosphere from reanalysis (Sec-
 563 tion 3.1) will be evaluated against in situ measurements at the surface (Section 3.2).

564 3.1 Remote sensed measurements

565 Two vertically-pointing Doppler radars are the primary remote-sensing instruments
 566 in this study. The 35 GHz Ka-band Zenith Radar (KAZR) and the 95 GHz Marine W-
 567 band cloud radar (MWACR) were deployed at Hyytiälä during the SNEX IOP. Due to a
 568 mispointing of MWACR, mean Doppler velocity measurements from that radar are not
 569 used in this study. It is important that KAZR and MWACR sampling volumes are broadly
 570 overlapping; both radar measurements are resampled from approximately 2 s to 120 s. Cal-
 561 ibration of MWACR and KAZR against a colocated vertically-pointing X-band radar is
 562 carried out as described in *Kneifel et al. [2015]*, after accounting for attenuation due to at-
 563 mospheric gases and liquid; when X-band radar is not available the most recent calibration
 564 is applied, and MWACR radar reflectivity is calibrated against KAZR radar reflectivity at
 565 cloud-top after correcting for attenuation.

567 Additional observations are available from the AMF2 high-spectral resolution lidar
 568 (HSRL), which measures molecular and particulate backscatter at 532 nm with gate spac-
 569 ing of 30 m and temporal resolution of 120 s. HSRL could be used for radar–lidar synergy
 570 retrievals of non-precipitating ice cloud, where the lidar provides valuable information
 571 on smaller ice particles and liquid droplets; however, in the rimed snow events of interest
 572 here the lidar is completely attenuated by liquid water near the surface. HSRL data are
 573 therefore presented alongside the radar data, but are not assimilated in the retrieval.

574 Microwave radiometer (MWR) measurements at 23.8 and 31.4 GHz are used to
575 retrieve liquid water path (LWP) and water vapour path [Cadeddu *et al.*, 2013]. While mi-
576 crowave radiometer measurements are not included in the retrieval, estimates of LWP pro-
577 vide information on the magnitude of supercooled liquid water (SLW) that are used to cor-
578 rect for radar attenuation due to liquid (discussed above and in Section 2.4) and to provide
579 context for the retrieval of riming based on the availability of supercooled liquid water in
580 mixed-phase clouds [e.g. Kalesse *et al.*, 2016; Moisseev *et al.*, 2017].

581 To assist in interpreting the remote-sensed data, atmospheric state profiles are ob-
582 tained from European Centre for Medium-Range Weather Forecasts (ECMWF) re-analysis
583 at 1 hour temporal resolution over the site. Variables are re-interpolated onto a height grid
584 using pressure measurements from 6 hourly radiosondes. Profiles of atmospheric temper-
585 ature, pressure and humidity are used in the target classification scheme and within the
586 retrieval algorithm to estimate radar attenuation due to atmospheric gases.

587 Prior to the retrieval remote-sensed and atmospheric data are averaged onto a com-
588 mon grid using the reflectivity-weighted mean Doppler velocity for averaging. A detection
589 mask is generated for each radar instrument, using the texture of the mean Doppler veloc-
590 ity [Helmus and Collis, 2016] and radar signal-to-noise ratio after subtracting an estimate
591 of the noise.

592 3.2 In situ measurements

593 The BAECC 2014 campaign provides a valuable opportunity to evaluate remote-
594 sensed estimates of snow against reliable and sustained in situ observations at the surface;
595 this is rarely possible at lower latitudes where both in situ and millimeter-wavelength radar
596 measurements are affected by melting. Images of ice particles from the precipitation imag-
597 ing package (PIP) video disdrometer [Newman *et al.*, 2009] are converted to measurements
598 of particle number concentration, size, area and fallspeed. The mass of each particle is
599 estimated from PIP observations of particle size, area and terminal velocity as described
600 in von Lerber *et al.* [2017]; the maximum dimension of the ice particles are scaled to de-
601 rive the particle masses that result in the best fit with snow accumulation measured by
602 nearby Pluvio snow gauges. PIP measurements at 5 min resolution are used, and shifted
603 by 5 minutes for comparison against remote-sensing measurements around 500 m above
604 ground level. Kneifel *et al.* [2015] discuss a more precise approach to estimating the time-

605 lag for evaluation against the lowest radar gates, but given the time-averaging used in this
606 retrieval a constant lag was sufficient.

607 The median diameter D_0 and normalized number concentration N_w parameters are
608 derived from the measured particle size distribution. Ice particle bulk density is estimated
609 from PIP measurements using the measured PSD and velocity-size relation, and estimated
610 mass-size relation according to (4) [von Lerber *et al.*, 2017]. This method was found to be
611 consistent with complementary methods using the Pluvio snow accumulation to estimate
612 the bulk density of ice [Tiira *et al.*, 2016; Moisseev *et al.*, 2017].

613 4 Results

614 We first demonstrate the retrieval for a case study (Sec. 4.1), before presenting statis-
615 tical evaluation of retrievals over 10 snow events during the SNEX IOP (Sec. 4.2).

616 4.1 Case study: February 21–22 2014

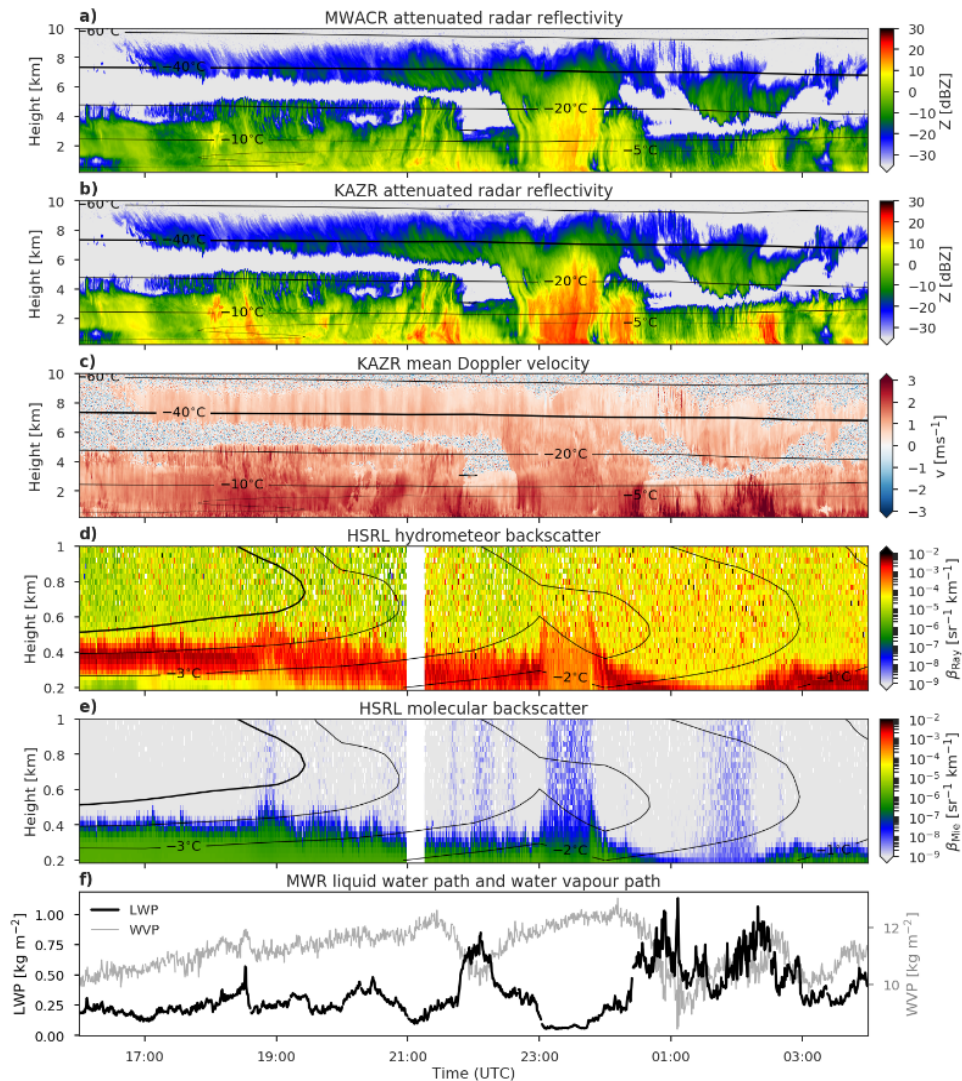
617 At 23:00 UTC on February 21 2014 a warm occluded front passed over Hyytiälä,
618 bringing about an hour of snow dominated by large aggregates. The light pre- and post-
619 frontal snow was characterised by rimed particles, including both heavily rimed aggregates
620 and graupel. With a total melted-equivalent accumulation of 5 mm comprising rimed and
621 unrimed snow, this event has been extensively studied with in situ [Tiira *et al.*, 2016; von
622 Lerber *et al.*, 2017; Moisseev *et al.*, 2017] and radar remote-sensing [Kneifel *et al.*, 2015;
623 Kalesse *et al.*, 2016] methods. The remote-sensed and in situ measurements for this case
624 are shown in Figs. 6 and 7, respectively. We divide the case into pre-frontal, frontal and
625 post-frontal regimes.

626 In the prefrontal regime (18:00 to 23:00 UTC) snowfall is relatively constant with
627 melted-equivalent rates between 0.2 and 1 mm h⁻¹ (Fig. 7d) from clouds with tops around
628 5 km and -20 °C (Fig. 6a–c). Particles measured in situ are dominated by a high concen-
629 tration of compact ice particles, with bulk densities between 200–400 kg m⁻³. PIP imagery
630 confirms the presence of graupel during this period [Fig. 14 from Kneifel *et al.*, 2015]. In
631 the hour prior to the front, cloud-top lowers to around 3 km and -15 °C, and relatively lit-
632 tle snow is measured at the surface. Moisseev *et al.* [2017] and von Lerber *et al.* [2017]
633 note that the low particle counts measured by PIP during this period lead to reduced con-
634 fidence in the retrieved quantities, and the bulk density (Fig. 7d) is not retrieved here.

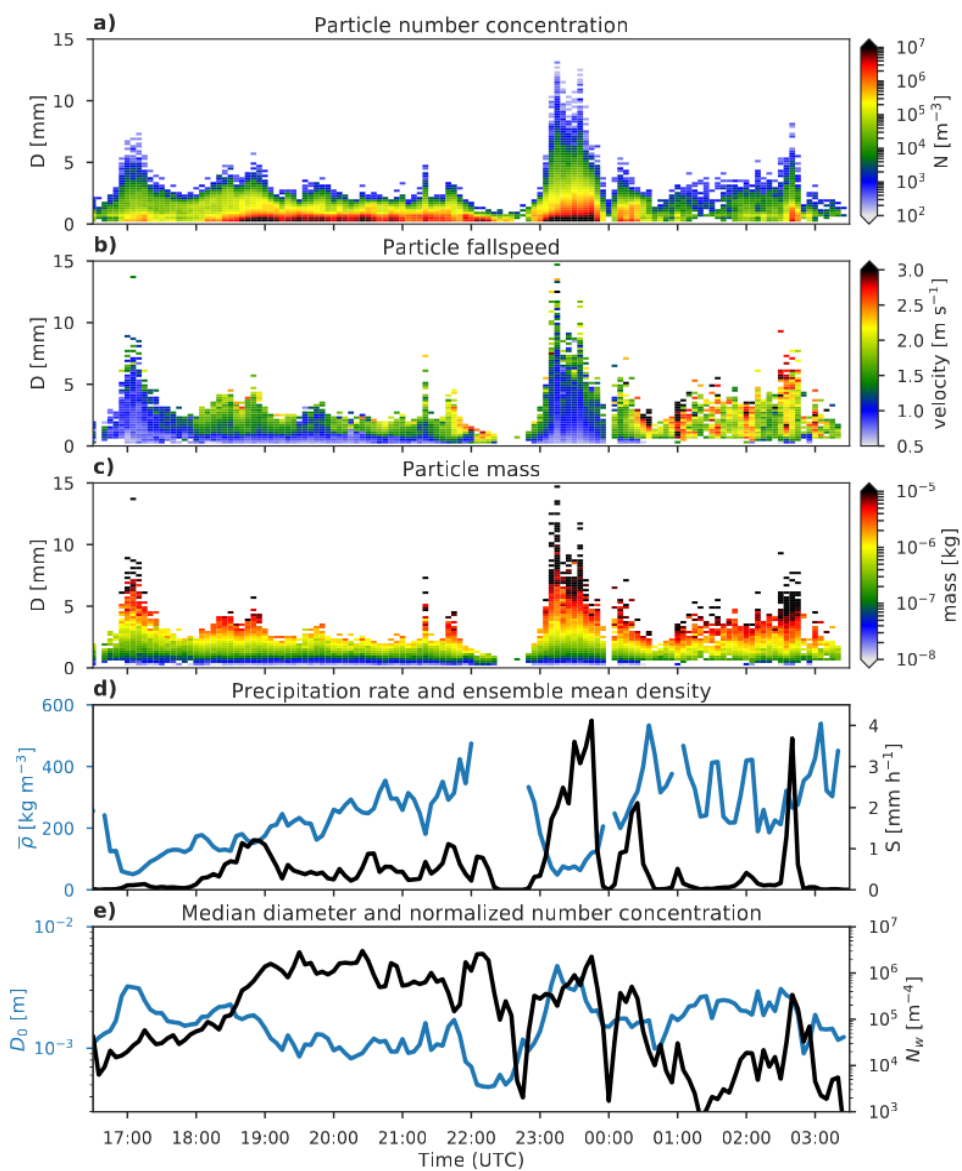
635 The frontal regime (23:00 and 00:00 UTC) brings heavier snow with a peak snow-
636 fall rate of 4.0 mm h^{-1} , and PIP imagery and measurements indicate large aggregates
637 with median diameters up to 5 mm (Fig. 7d); however, particle fallspeeds do not exceed
638 1.5 m s^{-1} (Fig. 7b). Here cloud-top is around 9 km and the maximum KAZR reflectivity
639 factor exceeds 20 dBZ near the surface.

640 The post-frontal regime (00:00 to 03:00 UTC) is dominated by patchy and very light
641 snow with the exception of two showers in which the snow rate exceeds 2 mm h^{-1} ; cloud-
642 top is again between 3 and 5 km. PIP measurements of bulk density are higher than in the
643 pre-frontal period, between 200 and 500 kg m^{-3} , and the particle size distribution confirms
644 that the post-frontal snow features a higher concentration of larger and fast-falling parti-
645 cles, which *von Lerber et al.* [2017] noted comprised a mixture of rimed aggregates and
646 graupel.

647 The presence of rimed snow and graupel throughout the pre- and post-frontal regimes
648 is indicative of persistent mixed-phase cloud layers in the lower atmosphere; however, the
649 vertical distribution of supercooled liquid water cannot be observed directly. The liquid
650 water path retrieved from microwave radiometer (Fig. 6f) and strong HSRL backscatter
651 (Fig. 6d) in the lowest liquid layers suggest that the vertically-integrated amount of liq-
652 uid water increases throughout the case, while the cloud base lowers. Above this lowest
653 layer, *Kalesse et al.* [2016] used Doppler spectra and soundings to infer the presence of
654 embedded mixed-phase cloud layers around 1 and 3.2 km. The exception is in the frontal
655 snow, when both microwave radiometer and lidar backscatter indicate that the liquid water
656 layers are depleted [*Moisseev et al.*, 2017]. Visual inspection of the mean Doppler veloc-
657 ity (Fig. 6c) hints at the signature of mixed-phase cloud layers in the reflectivity-weighted
658 average fallspeed of snow particles: the largest near-surface mean Doppler velocities cor-
659 respond in time to maxima in LWP around 22:00, 01:00 and 02:20 UTC (Fig. 6f) during
660 the pre- and post-frontal regimes, while the frontal regime represents a minimum in both
661 mean Doppler velocity and LWP despite being the period during which the greatest snow
662 rate and particle size are measured. Through the vertical profile, increases in the mean
663 Doppler velocity are evident at or around 1 and 3 km, which may be related to the on-
664 set of riming in mixed-phase cloud layers. A more quantitative estimate of riming will be
665 made using the CAPTIVATE retrieval algorithm.

Confidential manuscript submitted to *JGR-Atmospheres*

666 **Figure 6.** AMF2 measurements from Hyttiälä between 2014-02-21 16:00 UTC and 2014-02-22 03:00
 667 UTC. KAZR radar reflectivity (a) and mean Doppler velocity (b); MWACR radar reflectivity (c); HSRL atten-
 668 tuated Mie backscatter (d) and attenuated Rayleigh backscatter (e); and microwave radiometer LWP (f). Note
 669 the different vertical scales for HSRL backscatter (d & e). Black contours are temperature from ECMWF
 670 re-analysis; a darker line at -40°C denotes the temperature below which supercooled liquid water is not
 671 expected.

Confidential manuscript submitted to *JGR-Atmospheres*

672 **Figure 7.** In situ PIP measurements from Hyttiälä between 2014-02-21 16:00 UTC and 2014-02-22 05:00
 673 UTC. Particle size and fallspeed are measured, while particle mass, snow rate and bulk density are estimated
 674 as described in *von Lerber et al. [2017]*.

675 The CAPTIVATE retrieval is applied to the February 21 case, assimilating 35- and
 676 94-GHz radar reflectivities and 35-GHZ mean Doppler velocity (hereafter “ZZV”). Recall
 677 that the 94-GHz Doppler velocity is not used due to a mispointing error. The retrieved
 678 state variables are the extinction coefficient, primed number concentration and density in-
 679 dex (hereafter “ $\alpha_v N'_0 r'$ ”). As a check on the quality of the retrieval, we confirm that the
 680 best estimate of the state can be used to forward-model the observed MWACR radar re-
 681 flectivity (Fig. 8a&b) and KAZR mean Doppler velocity (Fig. 8c&d). Rather than report
 682 the values of the state variables directly, we derive more physically meaningful param-
 683 eters from the retrieval: the melted-equivalent snow rate (Fig. 8e), normalized number
 684 concentration (Fig. 8f), median diameter (Fig. 8g), and the density factor (Fig. 8h). In the
 685 prefrontal regime snow rate reaches 0.1–1.0 mm h⁻¹ below 3 km. In the frontal regime
 686 the snow rate exceeds 1 mm h⁻¹ between 5–7 km above ground level; toward the surface,
 687 number concentration decreases while median diameter increases, suggesting growth by
 688 aggregation. In the post-frontal showers maxima in snow rate correspond to streaks of in-
 689 creased number concentration and median diameter. Of primary interest is the retrieval
 690 of the density factor, which increases to around $r = 0.2$ below 3 km in the pre-frontal and
 691 post-frontal regimes and up to local maxima of 0.5 to 0.7 near the surface around 22:00,
 692 01:00 and 02:20 UTC; in short, the retrieved density factor maps closely to the regions of
 693 high mean Doppler velocity identified earlier. In the pre-frontal regime small but non-zero
 694 density factors are retrieved in both the cirrus and the midlevel cloud-tops, albeit with
 695 large estimated uncertainties (not shown); much of this cirrus occurs below temperatures
 696 at which supercooled liquid—and therefore riming—is to be expected (Fig. 6a–c), an oc-
 697 currence which has not been excluded within the retrieval. As discussed in Section 2.2.2,
 698 small non-zero density factors are within the observed variability of mass-size relations for
 699 unrimed particles; however it may also be the case that vertical air motion dominates the
 700 mean Doppler velocity in this regions.

701 **4.1.1 Profiles**

702 In addition to assimilating all available radar measurements and retrieving all state
 703 variables, it is of interest to explore the relative contributions of Doppler and dual-frequency
 704 measurements to the CAPTIVATE retrieval. These configurations are more easily com-
 705 pared at selected profiles, each representing 120 S of averaged radar measurements. We
 706 select a profile from each of the snow regimes: a pre-frontal profile at 21:30 UTC (Fig. 9

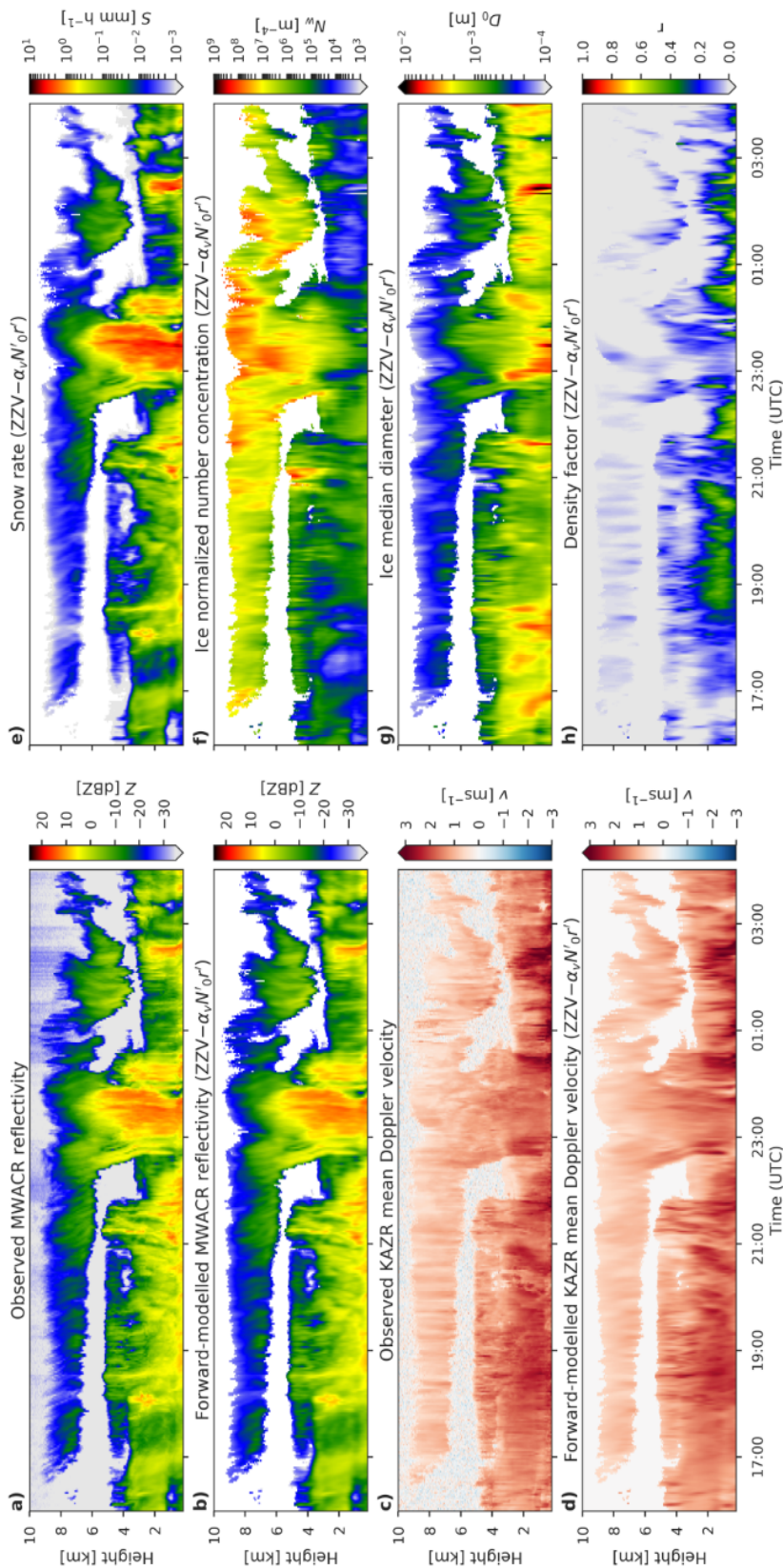
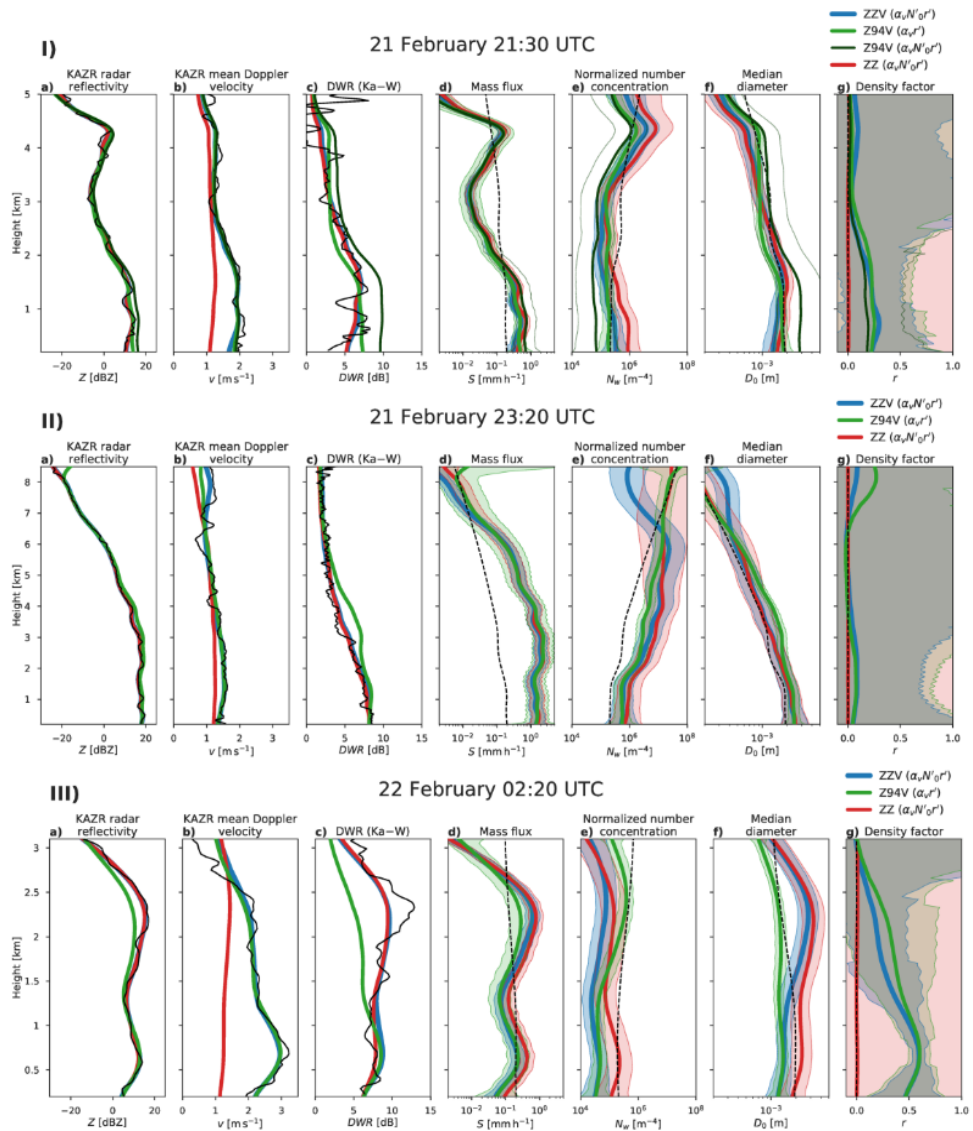


Figure 8. The observed and forward-modelled MWACR reflectivity (a & b), and observed and forward-modelled KAZR mean Doppler velocity (c & d); and the retrieved snow rate (e), normalized number concentration (f), median particle diameter (g) and density factor (h) from the ZZV retrieval for the 21 February 2014 case.

707 I), a frontal profile at 23:20 UTC (Fig. 9 II), and a post-frontal profile at 02:20 UTC (Fig. 9
708 III).

714 The $ZZV-\alpha_v N'_0 r'$ retrieval of the pre-frontal profile (Fig. 9 I) shows snow rate in-
715 creasing below 3 km to approximately 0.5 mm h^{-1} at the surface, concurrent with an in-
716 crease in the density factor to around $r = 0.3$ below 1 km. Large uncertainties in the re-
717 trieved density factor reflect a large observational uncertainty of 1 m s^{-1} in the Doppler
718 velocity; however, we find that the retrieved density factor is robust to changes in the ob-
719 servational uncertainty. When Doppler velocity is not assimilated ($ZZ-\alpha_v N'_0 r'$) there is lit-
720 tle constraint on the density factor, which remains close to $r = 0$. This leads to an under-
721 estimate in forward-modelled mean Doppler velocity of as much as 1 m s^{-1} below 2 km,
722 and N_w greater by a factor of 5 than that of $ZZV-\alpha_v N'_0 r'$; that is, when dense rimed par-
723 ticles are not retrieved, the lower density of ice is compensated by a larger concentration
724 of snow particles such that the snow rate differs only slightly from that of $ZZV-\alpha_v N'_0 r'$.
725 The $ZZ-\alpha_v N'_0 r'$ retrieval is very similar to one in which Doppler velocity is available,
726 but where all snow is assumed to be unrimed aggregates ($ZZV-\alpha_v N'_0$; not shown). Con-
727 versely, when only MWACR reflectivities are assimilated and the full state vector is re-
728 trieved ($Z94V-\alpha_v N'_0 r'$; the dark green line in Fig. 9 I), the PSD diverges significantly
729 from $ZZV-\alpha_v N'_0 r'$. A much lower number concentration of larger particles is retrieved,
730 with median diameter a factor of two larger than that of $ZZV-\alpha_v N'_0 r'$. Despite a lower
731 density factor, this retrieval appears well-constrained by the Doppler velocity—but the
732 forward-modelled DWR indicates that the larger particles lead to an error in Ka-band re-
733 flectivity of around 4 dB near the surface. This is an example of an under-constrained re-
734 trieval in which three state variables are estimated from two measured variables. A better-
735 posed retrieval can be made by treating the primed number concentration as a model vari-
736 able which does not vary from the prior $Z94V-\alpha_v r'$ (the bright green line in Fig. 9). The
737 results of this retrieval much more closely resemble $ZZV-\alpha_v N'_0 r'$, with reduced errors in
738 forward-modelled DWR and values of N'_0 and D_0 closer to their priors; therefore in subse-
739 quent profiles only the $Z94V-\alpha_v r'$ will be compared with $ZZV-\alpha_v N'_0 r'$ and $ZZ-\alpha_v N'_0 r'$.

740 In the frontal regime (Fig. 9 II) there is generally good agreement between retrievals,
741 which consistently represent a snow rate of 1 to 2 mm h^{-1} below 4 km; this relatively con-
742 stant mass flux corresponds with increasing median diameter and decreasing number con-
743 centration consistent with strong aggregation in the shower, and confirmed by the large
744 aggregate snowflakes observed at the surface (Fig. 7). Both ZZV and $Z94V$ diagnose



709 **Figure 9.** Forward-modelled measured variables and retrieved snow rate, normalized number concentra-
 710 tion, median diameter and density factor for ZZV, Z94V and ZZ retrievals, for a profile at 21:30 UTC (I),
 711 23:20 UTC (II) and 02:20 UTC (III) within the pre-frontal regime. Black solid lines indicate the observed
 712 variables, and dashed lines indicate the prior retrieved variables. Shading indicates the 5th to 95th
 713 uncertainty of the retrieval.

745 small non-zero density factors below about 4 km, without which ZZ under-estimates the
 746 mean Doppler velocity by around 0.5 m s^{-1} . In the mid-levels Z94V overestimates KAZR
 747 radar reflectivities, once again due to a smaller concentration of larger particles. In most
 748 other regards the retrievals are similar until near cloud-top, where relatively large Doppler
 749 velocities lead to the retrieval of small to moderate density factors in ZZV and Z94V
 750 which are unphysical (the contours in Fig. 6 indicate that the temperature is below -40°C
 751 at these heights), and may be a result of vertical air motion in the cirrus. In stratiform
 752 precipitation, the retrieval of dense ice due to small-scale turbulent features in vertical air
 753 motion is somewhat suppressed by the use of a Kalman smoother in the retrieval of the
 754 density index; however, it would also be possible within CAPTIVATE to reduce prior un-
 755 certainty in the density factor where riming is unlikely, or to apply higher uncertainties to
 756 mean Doppler velocity measurements where larger contributions from vertical air motion
 757 are expected.

758 In the postfrontal regime (Fig. 9 III) the Doppler velocity reaches 3 m s^{-1} below
 759 1 km, where ZZV and Z94V estimate density factors around $r = 0.6$; ZZ does not diag-
 760 nose resolve this increase in particle density, and the corresponding forward-modelled
 761 mean Doppler velocity differs from observations by almost 2 m s^{-1} along with overesti-
 762 mates in both number concentration and median size. While ZZV and Z94V converge
 763 upon similar PSDs below 1.5 km where the Doppler signal is strong, near the top of the
 764 cloud Z94V remains closer to its priors (recall that N'_0 does not vary in this retrieval),
 765 leading to a much higher concentration of small particles and a significant under-estimate
 766 of the KAZR radar reflectivity above 1.5 km.

767 While the uncertainties in the retrieved density factor are constrained in the parts of
 768 the profile where the mean Doppler velocity of denser particles differ significantly from
 769 that of unrimed aggregates—typically below 2 or 3 km in these profiles—very large den-
 770 sity factor uncertainties are evident aloft. In these regions the Doppler velocity contains
 771 little information about variations in density because the smallest particles are assumed to
 772 be solid quasi-spheroidal particles for all values of the density factor (see Fig. 3).

773 **4.1.2 Comparison against in situ measurements**

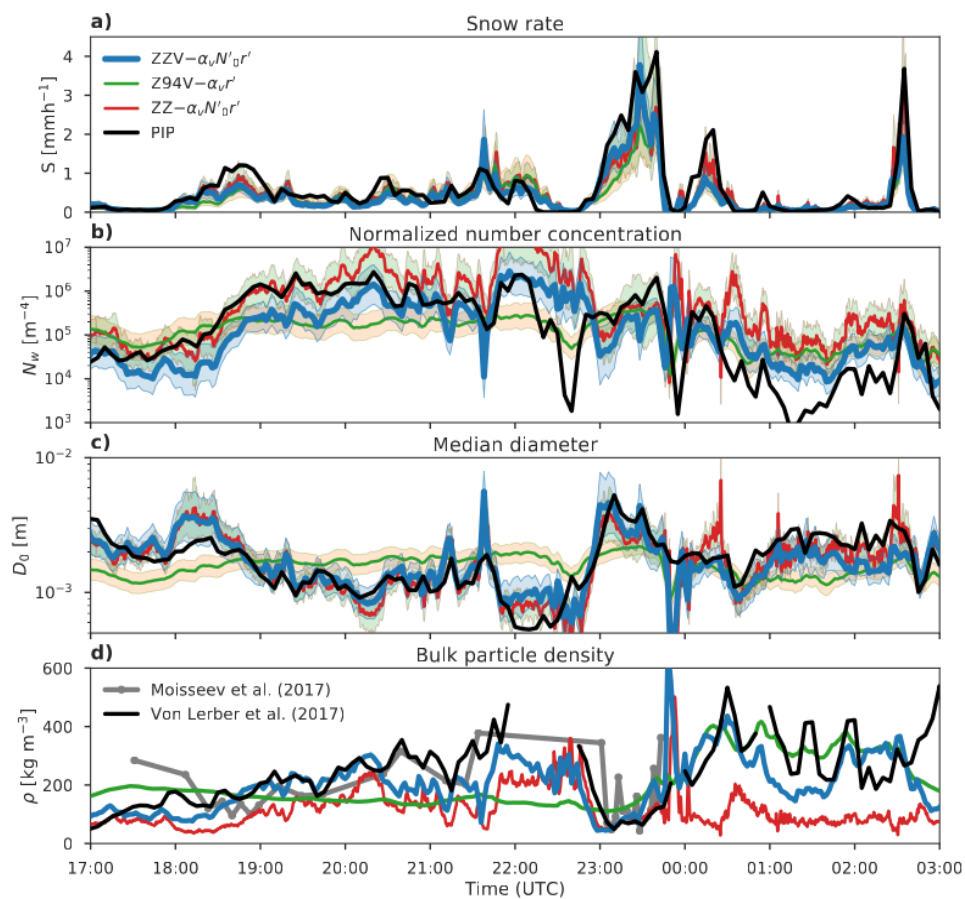
774 We now evaluate the CAPTIVATE retrievals against in situ measurements at the sur-
 775 face; ZZV, Z94V and ZZ estimates of snow rate, normalized number concentration, me-

776 dian diameter, and bulk density averaged over the radar gates up to 600 m above ground
777 level are compared against those from PIP (Fig. 10).

778 All of the CAPTIVATE retrievals of snow rate are within the range of uncertainty of
779 PIP snow rate, with under-estimates of up to 50 % especially evident in frontal and post-
780 frontal showers. As was also the case in the analysis of profiles, the estimated snow rates
781 are remarkably consistent between the different retrievals; this is despite significant differ-
782 ences in estimates of particle size, number concentration and density.

788 As they often compensate for one another, the parameters of the PSD are evaluated
789 together. ZZV and ZZ estimates of median diameter (Fig 10c) are within 50 % of PIP
790 measurements, and estimates of normalized number concentration (Fig 10b) are usually
791 within the retrieval uncertainty—with errors of up to a factor of five—of PIP measure-
792 ments. Without a dual-frequency constraint on particle size and therefore fewer state vari-
793 ables retrieved, the Z94V- $\alpha_v r'$ estimates of N'_0 and D_0 are less able to resolve the distinct
794 snow regimes: in the pre-frontal period Z94V number concentrations exceed PIP mea-
795 surements by up to an order of magnitude while particle sizes may be double the surface
796 observations; the inverse is true in the post-frontal period.

797 Finally we evaluate the retrieval against in situ measurements of bulk density (Fig. 10d).
798 The volume flux-weighted bulk density is estimated from retrieved particle properties con-
799 sistent with eq. 4, in which the mass- and velocity-size relations are modulated by the
800 retrieved density factor. We compare this remote-sensed estimate against two in situ re-
801 trievals of bulk density from PIP measurements [*von Lerber et al., 2017*] and a combina-
802 tion of PIP and Pluvio snow gauge measurements [*Moisseev et al., 2017*] to constrain the
803 total accumulation; we note that the former method was calibrated against the latter, so
804 these two retrievals are not independent. The retrieved density factor and median diam-
805 eter are both important to the estimated bulk density; when constrained by both Doppler
806 and dual-frequency measurements, ZZV is therefore broadly capable of resolving the bulk
807 density measured by PIP, although we note underestimates of 25–50 % between 20:30 and
808 22:00 in the pre-frontal period, and between 01:00 and 01:45 in the post-frontal period.
809 Errors in Z94V estimates of median diameter can either exacerbate (in the pre-frontal
810 regime) or mask (in the post-frontal) errors in the bulk density: as discussed above, with
811 a weaker constraint on particle size Z94V does not resolve the compact graupel ahead of
812 the front, and underestimates post-frontal particle size. Conversely, without Doppler infor-



783 **Figure 10.** Time series comparing mean retrieved variables over the lowest radar gates (between 300 m and
 784 600 m) against the in situ PIP measurements at the surface. Shaded areas indicate the 5th and 95th percentile
 785 uncertainty of the retrieval. Surface observations are shifted by 5 minutes. The bulk ice density is discontin-
 786 uous where very small median diameter leads to erroneously high densities, as discussed in *von Lerber et al.*
 787 [2017].

813 mation the bulk density estimates from ZZ are chiefly a function of particle size: density
814 rarely exceeds 200 kg m^{-3} except immediately ahead of the front, when median diameters
815 of less than 1 mm are estimated.

816 **4.1.3 Riming as an indicator of mixed-phase cloud**

817 While CAPTIVATE has been developed for radar–lidar–radiometer synergy retrievals,
818 in the present case the lidar is fully extinguished within less than 1 km of the surface in
819 the lowest of several shallow layers of mixed-phase cloud. Our retrievals assimilate radar
820 reflectivity and mean Doppler velocity, both of which are dominated by backscatter from
821 larger ice particles; the Doppler spectrum or its higher moments can sometimes be used to
822 identify the presence of liquid cloud [Kalesse *et al.*, 2016], although the broader applica-
823 bility of these methods can be limited, especially for retrievals from airborne and space-
824 borne platforms where spectral broadening is significant [e.g. Illingworth *et al.*, 2015].
825 The density of ice particles has been retrieved based on mean Doppler velocity, relying
826 on approximations to the morphology of ice particles from unrimed aggregates to graupel
827 and their associated terminal fallspeeds. We hypothesise that the primary process by
828 which high density factors occur is the riming of ice particles within mixed-phase clouds.
829 An independent source of information on the potential for riming is LWP retrieved from
830 the microwave radiometer; von Lerber *et al.* [2017] used LWP as a proxy for riming, and
831 the connection between LWP and rime mass fraction is also demonstrated from in situ re-
832 trievals in Moisseev *et al.* [2017].

833 For the present case, the timeseries of LWP is strongly correlated to the CAPTI-
834 VATE retrievals of density factor in the near-surface gates (Fig. 11a; $ZZV-\alpha_v N'_0 r'$). The
835 highest density factors correspond to the presence of significant mixed-phase cloud in
836 the pre- and post-frontal periods, and the dominance of unrimed aggregates to the de-
837 pletion of liquid evident during the frontal snow. The scatter plot of the LWP versus the
838 retrieved density factor (Fig. 11b) is coloured by the mean Doppler velocity and sized by
839 retrieved median diameter. At low LWP particles tend to be large unrimed aggregates with
840 mean Doppler velocities less than 2 m s^{-1} . Moderate LWP profiles correspond to parti-
841 cles ranging from larger rimed aggregates with $0.0 < r < 0.2$, to compact rimed aggre-
842 gates ($0.2 < r < 0.5$). At high LWP the snow is dominated by graupel ($0.5 < r < 0.8$),
843 with some instances of larger, fast-falling and heavily-rimed aggregates.

847 In summary, the February 21 2014 case study includes significant riming below
848 around 3 km during pre- and post-frontal snow, interrupted by a frontal shower dominated
849 by large aggregate snowflakes. Mean Doppler velocity provides an effective constraint on
850 estimates of the density factor, retrieved values of which varied from $r \approx 0.1$ for unrimed
851 aggregates $r \approx 0.6$ for graupel. Dual-frequency radar reflectivity proved critical to con-
852 straining estimates of the particle size distribution, leading to significant improvements in
853 retrieved quantities when compared with in situ measurements at the surface. While the
854 single-frequency retrieval was capable of similar estimates of snow rate and density fac-
855 tor, the retrieval was better constrained when a single parameter of the PSD was retrieved,
856 leading to estimates closer to the priors in which compact pre-frontal graupel was not re-
857 solved. Our hypothesis that the retrieved density factor varies chiefly due to the riming of
858 ice particles in mixed-phase cloud layers is supported by a strong association between the
859 density factor and an independent estimate of supercooled liquid water.

860 4.2 SNEX 2014 IOP

861 In this section the LWP is used as an indicator of the availability of SLW for rim-
862 ing, hence to distinguish between unrimed and rimed snow, and heavily rimed snow or
863 graupel. Snow events during the SNEX IOP were identified by *von Lerber et al.* [2017]
864 wherein significant snow was falling at the surface and the surface temperature was below
865 freezing (Table 3). A probability density function of LWP over the SNEX IOP (Fig. 12a)
866 illustrates that, while the majority of the snow events during the period occurred in low-
867 LWP conditions, significant SLW is relatively frequent during the IOP. Following a similar
868 distinction made in *von Lerber et al.* [2017], three ranges of LWP are used to distinguish
869 between unrimed ($LWP < 0.1 \text{ kg m}^{-2}$), moderately rimed ($0.1 \leq LWP < 0.3 \text{ kg m}^{-2}$),
870 and heavily rimed snow or graupel ($LWP \geq 0.3 \text{ kg m}^{-2}$). In that study the mass-size and
871 fallspeed-size relations from in situ measurements of particles were shown to be consis-
872 tent with the LWP classification. Unrimed snow accounts for just over half of the profiles;
873 rimed snow around 30 %, and graupel around 10 %; in the rest, no significant snow was
874 measured and the profile was skipped. While the unrimed snow is associated with the
875 coldest surface temperatures (Fig. 12b) on average, all three categories are most frequent
876 at temperatures just below freezing; it is not evident that the riming events can be distin-
877 guished by temperature. Similarly, the low-LWP regime includes almost all events with

880

Table 3. Snow events during SNEX 2014 IOP

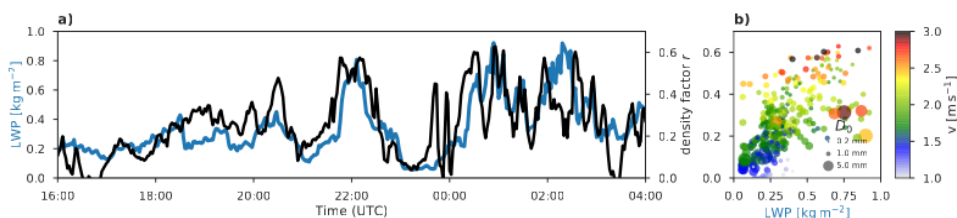
Date (UTC) 2014	Melted-equivalent accumulation [mm]	Surface temperature (°C)	
		Min	Max
*1 Feb 00:00—06:00	7.4	-9.8	-8.9
*1 Feb 10:00—16:00	1.4	-7.9	-7.0
2 Feb 16:00—19:00	1.7	-5.4	-5.2
12 Feb 04:00—09:00	0.8	-1.0	0.0
15 Feb 21:00—16 Feb 02:00	2.6	-2.1	-1.0
21 Feb 16:00—22 Feb 03:30	5.0	-2.7	0.0
15 Mar 05:00—07:00	0.3	-2.0	-1.3
*18 Mar 08:00—19:00	4.4	-3.8	-1.8
19 Mar 00:00—20:00	1.5	-7.3	-3.7
20 Mar 16:00—00:00	6.1	-4.3	-1.3

* Denotes events where dual-frequency radar data were not always available.

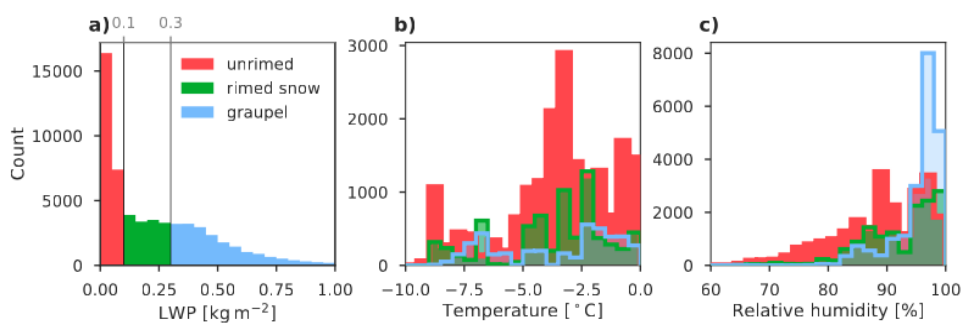
878 low relative humidities (Fig. 12c), but all categories occur most frequently at relative hu-
879 midities greater than around 90 %.

883 The CAPTIVATE best estimate ($ZZV-\alpha_v N'_0 r'$) was run over approximately 55 hours
884 of available dual-frequency Doppler radar data. Joint histograms of the profile of forward-
885 modelled observed variables and retrieved variables are shown for each of the LWP classi-
886 fications (Fig. 13).

887 The unrimed snow (Fig. 13-I; $LWP < 0.1 \text{ kg m}^{-3}$) is associated with the lowest
888 mean Doppler velocities (Fig. 13-Ib), which average around 1 m s^{-1} near the surface and
889 never exceed 2 m s^{-1} . The corresponding median density factor (Fig. 13-Ig) is between
890 0 and 0.2 below 4 km; this is consistent with the finding of *Moissev et al.* [2017] that
891 the mass-size of unrimed aggregate snow at Hyytiälä is consistently higher than that of
892 *Brown and Francis* [1995], corresponding to roughly $r = 0.15$ in Fig. 1. In the earlier pro-
893 file of unrimed snow (Fig. 9 II) it was noted that ice water content remained constant with
894 height near the surface while diameter increased and number concentration decreased;
895 these characteristic features of aggregation are robustly present in approximately 30 hours



844 **Figure 11.** Time series (a) and scatter plot (b) of $ZZV-\alpha_v N'_0 r'$ density factor in the lowest radar gates
 845 (300m to 600m) against LWP measured by the microwave radiometer. In the scatter plot the markers are
 846 coloured by the mean Doppler velocity, and sized according to the retrieved median diameter.



881 **Figure 12.** Histograms of remote-sensed LWP (a) and surface temperature (b) and relative humidity (c)
 882 data from all snow events from SNEX IOP, grouped into three LWP classes.

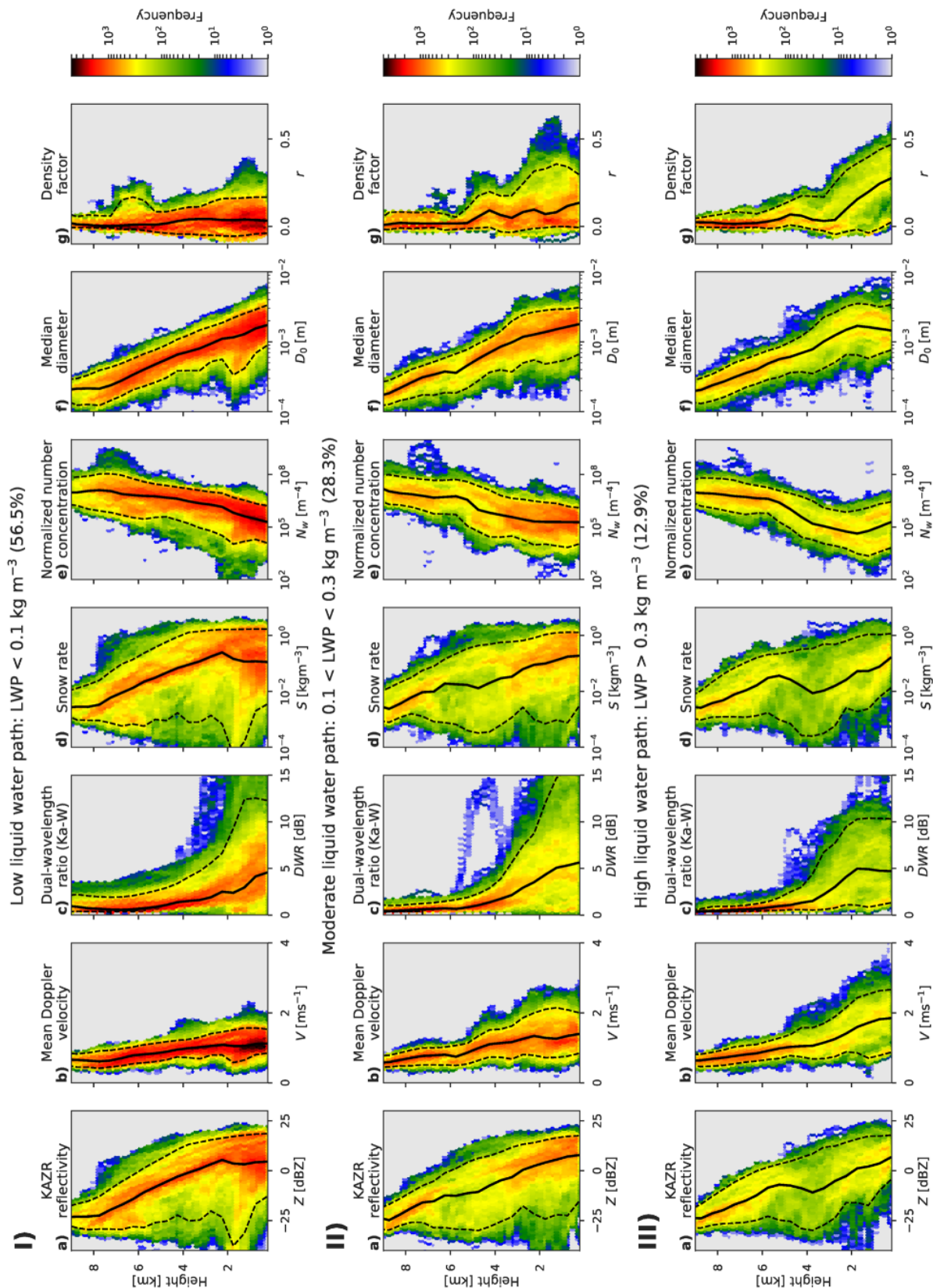


Figure 13. Joint histograms for $ZZV-\alpha_v N'_0 r'$ CAPTIVATE retrieval of forward-modelled (a–c) and retrieved (d–g) variables against altitude for snow events during the SNEX 2014 IOP. Snow events are divided into three regimes, unrimed snow (I), rimed snow (II) and graupel (III), using LWP as a proxy for riming. Solid black lines indicate the median—and dashed lines the 5th and 95th percentiles—of the forward modelled or retrieved values at each height.

896 of aggregate snowfall, with the median snow rate (Fig. 13-Id) constant below 3 km, con-
897 current with an increase in median size (Fig. 13-If) and a decrease in number concen-
898 tration (Fig. 13-Ie) toward the surface. The gradient in D_0 represents roughly a doubling
899 in median particle diameter over 2 km. The Ka-W dual-wavelength ratio increases below
900 3 or 4 km to a median of around 5 dB; however, comparison to the triple-frequency data
901 (Fig. 5) shows that values in this range are not unique to either aggregates or graupel;
902 a third radar frequency would provide valuable information to help constrain a retrieval
903 based on the different scattering signatures of unrimed aggregates and heavily rimed parti-
904 cles.

905 In the rimed snow (Fig. 13 II; $0.1 \leq LWP < 0.3 \text{ kg m}^{-3}$) mean Doppler velocities
906 (Fig. 13IIb) are between 1 and 2 m s^{-1} near the surface, corresponding to density factors
907 that increase below about 4 km to between 0 and 0.4 in the lowest 2 km. Unlike the un-
908 rimed snow, the snow rate (Fig. 13 IId) continues to increase toward the surface, indicat-
909 ing an addition of ice water content which may be due to accretion of supercooled liquid
910 or vapour deposition. The near-surface gradients of N'_0 and D_0 (Fig. 13 IIe & f) are not
911 significantly reduced from those in unrimed snow, so it seems likely that a mix of aggre-
912 gation, riming and deposition processes occur within this regime.

913 Finally, the heavily rimed snow or graupel (Fig. 13 III; $LWP \geq 0.3 \text{ kg m}^{-3}$) is as-
914 sociated with mean Doppler velocities (Fig. 13 IIIb) up to 3 m s^{-1} and density factors
915 (Fig. 13 IIIg) increasing steeply below 3 km up to as much as $r = 0.5$ with a median around
916 $r = 0.3$. Unlike the unrimed and rimed snow regimes, the snow rate in this regime in-
917 creases rapidly toward the surface, with the median snow rate increasing by an order of
918 magnitude over the lowest 2 to 3 km—a rate similar to that in the upper-level clouds of
919 all regimes—however, D_0 and N'_0 are near-constant in the lower levels. This is consistent
920 with an accretion of mass due to riming, although deposition cannot be ruled out. An in-
921 crease in normalized number concentration may be discernible near the surface (Fig. 13
922 IIIg), perhaps suggesting a relative increase in the concentration of small particles, or a
923 breakup of larger particles. This may be indicative of a secondary ice generation process
924 such as rime splintering; however, more work would be required to confirm this, and to
925 what degree the present retrieval may help in the study of secondary ice processes.

926 An evaluation of the CAPTIVATE retrieval over all available dual-frequency Doppler
927 radar data from the SNEX IOP has shown characteristic differences between the profiles

928 of snow rate, PSD parameters and density factor between profiles of unrimed and rimed
929 snow. LWP provides a suitable proxy to distinguish between unrimed and heavily rimed
930 snow events. This initial analysis has focused on demonstrating the potential to resolve
931 key microphysical processes from the Doppler velocity; however, many other analyses of
932 the meteorological and thermodynamical context of riming and aggregation processes may
933 be envisaged.

934 **5 Discussion and conclusions**

935 The morphology of an ice particle is a record of the microphysical processes by
936 which it forms; in this study we have proposed a simple parameterisation for the repre-
937 sentation of the wide range of ice particle densities and shapes from unrimed aggregate
938 snowflakes to graupel and hail. Remote-sensed estimates of snow typically assume snow
939 particles that resemble unrimed aggregates; however, riming is both a critical process for
940 surface hydrology and a control on radiatively-important mixed-phase clouds which are
941 difficult to remote-sense and poorly represented in numerical models. We have demon-
942 strated a method for diagnosing riming within the framework of CAPTIVATE, an optimal
943 estimation algorithm for radar-lidar-radiometer retrievals of clouds, aerosols and precipita-
944 tion.

945 The retrieved density factor modulates the density, shape and radar scattering cross-
946 section of ice particles, and is chiefly inferred from mean Doppler velocity, a measure of
947 reflectivity-weighted particle terminal velocities. Many refinements to this parameterisa-
948 tion may be envisaged to better represent the microphysical processes in question, and
949 the sensitivity of the retrieval to the formulation of the density factor and its effect on the
950 mass, area and scattering cross-sections of ice particles requires further study. An alterna-
951 tive parameterisation intended to more closely resemble the conceptual model for the rim-
952 ing of aggregate snowflakes was tested using a reference mass-size relation for unrimed
953 aggregates at Hyttiälä [von Lerber *et al.*, 2017] with a constant exponent of $b_m = 2.1$, and
954 where only the prefactor of the mass-size relation was scaled with the density factor. This
955 representation is more consistent with the conceptual model of the “in-filling” stage of
956 riming, but does not encompass the observed variability amongst unrimed snowflakes or
957 the higher exponents of heavily rimed graupel-like particles. The retrieved snow rate and
958 PSD were not strongly sensitive to changes in how particle density is allowed to vary, sug-
959 gesting the two parameterisations allow for similar representation of unrimed to lightly

960 rimed aggregates despite some change in the mass-size exponent; however, in situ mea-
961 surements of snow rate and bulk particle density agreed better with the original retrieval
962 in the densest post-frontal snow, suggesting the advantages of representing a broader range
963 of particle morphologies, especially of heavily rimed graupel-like particles. Our prior den-
964 sity factor of $r = 0$ relates to the unrimed aggregates of *Brown and Francis* [1995], but
965 it may be possible to implement more sophisticated priors or constraints on the retrieval
966 based on the atmospheric state [e.g. *Lin and Colle*, 2011; *Szyrmer and Zawadzki*, 2014a],
967 or from regional climatologies, to better resolve this variability; for example, *Moisseev*
968 *et al.* [2017] showed that the lowest-density particles at Hyttiälä were significantly more
969 dense than those of *Brown and Francis* [1995], and this could be represented with an up-
970 dated prior of $r \approx 0.15$ near the surface. Concurrent remote-sensed and in situ measure-
971 ments from the BAECC 2014 campaign have provided an invaluable opportunity to eval-
972 uate retrievals of rimed snow. Sustained particle imaging and multiple-frequency radar
973 measurements from Hyttiälä and other ARM and CloudNet “supersites” will provide criti-
974 cal datasets for the improved representation of snow microphysics, as well as validation for
975 future satellite retrievals.

976 The CAPTIVATE retrieval was applied to vertically-pointing Ka- and W-band Doppler
977 radar measurements from 10 snow events over the SNEX IOP of BAECC 2014. Dual-
978 frequency and Doppler radar measurements provided sufficient information to retrieve two
979 parameters of the PSD as well as the density factor. The dual-frequency radar reflectiv-
980 ities and mean Doppler velocity make distinct contributions to the retrieval, with radar
981 reflectivities at Ka- and W bands providing a strong constraint on the particle size dis-
982 tribution but relatively little information on density; Doppler velocity provided the sole
983 constraint on the density factor. Estimates of near-surface snow rate were within 50 % of
984 in situ measurements both with and without Doppler and dual-frequency measurements,
985 showing a remarkably robust retrieval of ice water content from 94-GHz radar reflectivity;
986 however, to accurately estimate the parameters of the PSD as well as the bulk ice density,
987 it was important to have both dual-frequency and Doppler information. With the recent
988 availability of multiple-frequency Doppler radar observations of snow, and supported by
989 observational and theoretical insights into the triple-frequency signatures of rimed and un-
990 rimed ice [e.g. *Kneifel et al.*, 2018], it will become increasingly important to quantify the
991 information content of each additional observational variable within an optimal estimation
992 framework.

993 The retrieval of riming provides an indirect insight into the presence of supercooled
994 liquid water, and it may hence be possible to use spaceborne Doppler radars to better
995 quantify the frequency and distribution of embedded mixed-phase clouds—at least where
996 precipitating ice is present. Using LWP as a proxy for riming provided a robust distinction
997 between retrieved snow profiles of unrimed aggregates, rimed aggregates and graupel; no
998 such clear distinction was evident in surface temperature or relative humidity. For profiles
999 with low LWP the dominant growth process near the surface was aggregation, while in
1000 high-LWP conditions the accretion of ice mass due to riming was evident. The ability to
1001 distinguish between microphysical processes through the profile suggests the potential for
1002 using multiple-frequency and Doppler radars to estimate rime mass content and relate it
1003 to the budget of supercooled liquid [e.g. *Moisseev et al.*, 2017], as well as to estimate mi-
1004 crophysical process rates [e.g. *Mace and Benson*, 2017]. These features were best resolved
1005 in retrievals combining dual-frequency and Doppler measurements; however, the onset of
1006 riming was also reliably detected with single-frequency radar retrievals, which could be
1007 sufficient to provide improved insights into the position of embedded mixed-phase layers
1008 within optically thick ice clouds from space.

1009 In the mixed-phase cloud situations in which riming occurs, ground-based lidars
1010 are quickly attenuated by liquid water near the surface. Therefore it was not possible in
1011 this study to exploit radar–lidar synergy, either for the retrieval of ice [e.g. *Delanoë and*
1012 *Hogan*, 2010] or for a simultaneous estimate of ice and liquid; instead a correction for liq-
1013 uid attenuation was applied to the radar reflectivity, and the retrieval carried out only for
1014 ice. LWP estimates from a co-located microwave radiometer were combined with an as-
1015 sumption about the vertical distribution of liquid water to estimate the radar attenuation
1016 as a pre-processing step before the radar retrieval. A more satisfactory approach within
1017 the optimal estimation retrieval framework would be to include a microwave radiometer
1018 forward model and perform a synergy retrieval, building upon studies into the active and
1019 passive microwave scattering of snow [e.g. *Kneifel et al.*, 2010]. This would provide addi-
1020 tional constraints on retrievals of cloud and precipitation to those provided by other pas-
1021 sive shortwave and longwave radiances [e.g. *Leinonen et al.*, 2016] or path-integrated at-
1022 tenuation from surface radar backscatter [e.g. *Haynes et al.*, 2009; *Hawkness-Smith*, 2010].

1023 The CAPTIVATE retrieval has been developed for the synergy of EarthCARE’s 94-
1024 GHz cloud profiling Doppler radar [*Illingworth et al.*, 2015] with high-spectral resolution
1025 atmospheric lidar and multi-spectral imaging radiometer. The capabilities of multiple-

1026 frequency Doppler radars—as well as synergies with a range of active and passive mea-
1027 surements including microwave radiometers—are also of interest. In this study we have
1028 considered the contribution of Doppler velocity and dual-frequency radars to the optimal
1029 estimation of snow, following a previous study using airborne dual-frequency Doppler
1030 radars for CAPTIVATE retrievals of tropical rain [Mason *et al.*, 2017]. Retrievals assim-
1031 ilating both dual-frequency and Doppler radar measurements to retrieve two parameters of
1032 the ice PSD and the density factor performed best, producing estimates of particle number
1033 concentration, size and bulk density near the surface that were close to in situ measure-
1034 ments. A single-frequency Doppler radar was best constrained when retrieving a single
1035 parameter of the PSD; however, we demonstrated that such a retrieval was sufficient to
1036 diagnose rimed snow in stratiform snow—wherein the mean Doppler velocity can be as-
1037 sumed to be dominated by hydrometeor fallspeed and not vertical air motion—and that the
1038 retrieval is robust to large observational uncertainties. The many challenges of making use
1039 of Doppler velocity measurements from space—including vertical resolution, horizontal
1040 averaging [e.g. Kollias *et al.*, 2014], ground clutter, and radar mispointing [e.g. Battaglia
1041 and Kollias, 2015]—have not been considered here, and work is ongoing to apply radar
1042 simulators to airborne and ground-based measurements or numerical models to better un-
1043 derstand the outlook for retrievals from EarthCARE [e.g. Battaglia and Tanelli, 2011]. Be-
1044 yond EarthCARE, the prospect of spaceborne multiple-frequency Doppler radars [National
1045 Academies of Sciences Engineering and Medicine, 2018] provides opportunities for further
1046 advancements in the global remote-sensing of ice, including estimates of the morphology
1047 and microphysics of snow and insights into mixed-phase clouds.

1048 **Acknowledgments**

1049 We thank three anonymous reviewers for motivating significant improvements to this study,
1050 and Chris Westbrook for helpful discussions throughout. Alessio Bozzo is thanked for his
1051 contribution to the development of the CAPTIVATE software. This work is supported by
1052 the National Centre for Earth Observation (NCEO) and European Space Agency Grant 4000112030/15/NL/CT,
1053 with computing resources provided by the University of Reading. C. Chiu is funded by
1054 the Office of Science (BER), DOE under grant DE-SC0011666. D. Moisseev acknowl-
1055 edges the funding received by ERA-PLANET, trans-national project iCUPE (Grant Agree-
1056 ment no. 689443), funded under the EU Horizon 2020 Framework Programme and Academy
1057 of Finland (grants 307331 and 305175). Contributions by S. Kneifel were carried out

1058 within the Emmy-Noether Group OPTIMIce funded by the German Science Foundation
1059 (DFG) under Grant KN 1112/2-1.

1060 BAECC 2014 radar data are available from the ARM data archive (www.arm.gov/data),
1061 and PIP particle measurements for two years at Hyytiälä can be accessed at github
1062 (github.com/dmoisseev/Snow-Retrievals-2014-2015).

1063 References

- 1064 Battaglia, A., and P. Kollias (2015), Using Ice Clouds for Mitigating the EarthCARE
1065 Doppler Radar Mispointing, *IEEE Transactions on Geoscience and Remote Sensing*,
1066 53(4), 2079–2085, doi:10.1109/TGRS.2014.2353219.
- 1067 Battaglia, A., and S. Tanelli (2011), DOMUS: DOPpler MULTiple-Scattering Simu-
1068 lator, *IEEE Transactions on Geoscience and Remote Sensing*, 49(1), 442–450, doi:
1069 10.1109/TGRS.2010.2052818.
- 1070 Brown, P. R. A., and P. N. Francis (1995), Improved Measurements of the Ice Water Con-
1071 tent in Cirrus Using a Total-Water Probe, *Journal of Atmospheric and Oceanic Technol-
1072 ogy*, 12(2), 410–414, doi:10.1175/1520-0426(1995)012<0410:IMOTIW>2.0.CO;2.
- 1073 Cadeddu, M. P., J. C. Liljegren, and D. D. Turner (2013), The Atmospheric radiation mea-
1074 surement (ARM) program network of microwave radiometers: instrumentation, data,
1075 and retrievals, *Atmospheric Measurement Techniques*, 6(9), 2359–2372, doi:10.5194/amt-
1076 6-2359-2013.
- 1077 Casella, D., G. Panegrossi, P. Sandò, A. C. Marra, S. Dietrich, B. T. Johnson, and
1078 M. S. Kulie (2017), Evaluation of the GPM-DPR snowfall detection capabil-
1079 ity: Comparison with CloudSat-CPR, *Atmospheric Research*, 197, 64–75, doi:
1080 10.1016/J.ATMOSRES.2017.06.018.
- 1081 Ceccaldi, M., J. Delanoë, R. J. Hogan, N. L. Pounder, A. Protat, and J. Pelon (2013),
1082 From CloudSat-CALIPSO to EarthCare: Evolution of the DARDAR cloud classifica-
1083 tion and its comparison to airborne radar-lidar observations, *Journal of Geophysical Re-
1084 search: Atmospheres*, 118(14), 7962–7981, doi:10.1002/jgrd.50579.
- 1085 Cesana, G., J. E. Kay, H. Chepfer, J. M. English, and G. de Boer (2012), Ubiqui-
1086 tous low-level liquid-containing Arctic clouds: New observations and climate model
1087 constraints from CALIPSO-GOCCP, *Geophysical Research Letters*, 39(20), doi:
1088 10.1029/2012GL053385.

- 1089 Chen, S., Y. Hong, M. Kulie, A. Behrangi, P. M. Stepanian, Q. Cao, Y. You, J. Zhang,
1090 J. Hu, and X. Zhang (2016), Comparison of snowfall estimates from the NASA Cloud-
1091 Sat Cloud Profiling Radar and NOAA/NSSL Multi-Radar Multi-Sensor System, *Journal*
1092 *of Hydrology*, *541*, 862–872, doi:10.1016/j.jhydrol.2016.07.047.
- 1093 Delanoë, J., and R. J. Hogan (2010), Combined CloudSat-CALIPSO-MODIS retrievals
1094 of the properties of ice clouds, *Journal of Geophysical Research: Atmospheres*, *115*(4),
1095 D00H29, doi:10.1029/2009JD012346.
- 1096 Delanoë, J., A. Protat, J. Testud, D. Bouniol, A. J. Heymsfield, A. Bansemer, P. R. A.
1097 Brown, and R. M. Forbes (2005), Statistical properties of the normalized ice par-
1098 ticle size distribution, *Journal of Geophysical Research*, *110*(D10), D10,201, doi:
1099 10.1029/2004JD005405.
- 1100 Delanoë, J. M. E., and R. J. Hogan (2008), A variational scheme for retrieving ice cloud
1101 properties from combined radar, lidar, and infrared radiometer, *Journal of Geophysical*
1102 *Research*, *113*(D7), D07,204, doi:10.1029/2007JD009000.
- 1103 Delanoë, J. M. E., A. J. Heymsfield, A. Protat, A. Bansemer, and R. J. Hogan (2014),
1104 Normalized particle size distribution for remote sensing application, *Journal of Geo-*
1105 *physical Research: Atmospheres*, *119*(7), 4204–4227, doi:10.1002/2013JD020700.
- 1106 Erfani, E., and D. L. Mitchell (2017), Growth of ice particle mass and projected area dur-
1107 ing riming, *Atmospheric Chemistry and Physics*, *17*(2), 1241–1257, doi:10.5194/acp-17-
1108 1241-2017.
- 1109 Field, P. R., and A. J. Heymsfield (2015), Importance of snow to global precipitation,
1110 *Geophysical Research Letters*, *42*(21), doi:10.1002/2015GL065497.
- 1111 Field, P. R., R. J. Hogan, P. R. A. Brown, A. J. Illingworth, T. W. Choullarton, and R. J.
1112 Cotton (2005), Parametrization of ice-particle size distributions for mid-latitude strat-
1113 iform cloud, *Quarterly Journal of the Royal Meteorological Society*, *131*(609), 1997–
1114 2017, doi:10.1256/qj.04.134.
- 1115 Field, P. R., A. J. Heymsfield, and A. Bansemer (2007), Snow Size Distribution Parame-
1116 terization for Midlatitude and Tropical Ice Clouds, *Journal of the Atmospheric Sciences*,
1117 *64*(12), 4346–4365, doi:10.1175/2007JAS2344.1.
- 1118 Francis, P. N., P. Hignett, and A. Macke (1998), The retrieval of cirrus cloud prop-
1119 erties from aircraft multi-spectral reflectance measurements during EUCREX'93,
1120 *Quarterly Journal of the Royal Meteorological Society*, *124*(548), 1273–1291, doi:
1121 10.1002/qj.49712454812.

- 1122 Fujiyoshi, Y., and G. Wakahama (1985), On Snow Particles Comprising an Aggre-
1123 gate, *Journal of the Atmospheric Sciences*, 42(15), 1667–1674, doi:10.1175/1520-
1124 0469(1985)042<1667:OSPCAA>2.0.CO;2.
- 1125 Grazioli, J., G. Lloyd, L. Panziera, C. R. Hoyle, P. J. Connolly, J. Henneberger, and
1126 A. Berne (2015), Polarimetric radar and in situ observations of riming and snowfall
1127 microphysics during CLACE 2014, *Atmospheric Chemistry and Physics*, 15(23), 13,787–
1128 13,802, doi:10.5194/acp-15-13787-2015.
- 1129 Grecu, M., W. S. Olson, S. J. Munchak, S. Ringerud, L. Liao, Z. Haddad, B. L. Kelley,
1130 and S. F. McLaughlin (2016), The GPM Combined Algorithm, *Journal of Atmospheric*
1131 *and Oceanic Technology*, 33(10), 2225–2245, doi:10.1175/JTECH-D-16-0019.1.
- 1132 Harimaya, T., and M. Sato (1989), Measurement of the Riming Amount on Snowflakes,
1133 *Journal of the Faculty of Science, Hokkaido University. Series 7, Geophysics*, 8(4), 355–
1134 366.
- 1135 Hawkness-Smith, L. (2010), A novel retrieval of liquid water path and a evaluation of the
1136 representation of drizzle in numerical models, Ph.D. thesis, University of Reading.
- 1137 Haynes, J. M., T. S. L'Ecuyer, G. L. Stephens, S. D. Miller, C. Mitrescu, N. B. Wood,
1138 and S. Tanelli (2009), Rainfall retrieval over the ocean with spaceborne W-band radar,
1139 *Journal of Geophysical Research*, 114, D00A22, doi:10.1029/2008JD009973.
- 1140 Helmus, J. J., and S. M. Collis (2016), The Python ARM Radar Toolkit (Py-ART), a Li-
1141 brary for Working with Weather Radar Data in the Python Programming Language,
1142 *Journal of Open Research Software*, 4(1), doi:10.5334/jors.119.
- 1143 Heymsfield, A. J. (1982), A Comparative Study of the Rates of Development of Potential
1144 Graupel and Hail Embryos in High Plains Storms, *Journal of the Atmospheric Sciences*,
1145 39(12), 2867–2897, doi:10.1175/1520-0469(1982)039<2867:ACSOTR>2.0.CO;2.
- 1146 Heymsfield, A. J., and M. Kajikawa (1987), An Improved Approach to Calculating Termi-
1147 nal Velocities of Plate-like Crystals and Graupel, *Journal of the Atmospheric Sciences*,
1148 44(7), 1088–1099, doi:10.1175/1520-0469(1987)044<1088:AIATCT>2.0.CO;2.
- 1149 Heymsfield, A. J., and L. M. Miloshevich (2003), Parameterizations for the
1150 Cross-Sectional Area and Extinction of Cirrus and Stratiform Ice Cloud Parti-
1151 cles, *Journal of the Atmospheric Sciences*, 60(7), 936–956, doi:10.1175/1520-
1152 0469(2003)060<0936:PFTCSA>2.0.CO;2.
- 1153 Heymsfield, A. J., and C. D. Westbrook (2010), Advances in the Estimation of Ice Parti-
1154 cle Fall Speeds Using Laboratory and Field Measurements, *Journal of the Atmospheric*

Confidential manuscript submitted to *JGR-Atmospheres*

- 1155 *Sciences*, 67(8), 2469–2482, doi:10.1175/2010JAS3379.1.
- 1156 Heymsfield, A. J., C. Schmitt, A. Bansemer, and C. H. Twohy (2010), Improved Representa-
1157 tion of Ice Particle Masses Based on Observations in Natural Clouds, *Journal of the*
1158 *Atmospheric Sciences*, 67(10), 3303–3318, doi:10.1175/2010JAS3507.1.
- 1159 Heymsfield, A. J., S. Y. Matrosov, and N. B. Wood (2016), Toward Improving Ice Wa-
1160 ter Content and Snow-Rate Retrievals from Radars. Part I: X and W Bands, Empha-
1161 sizing CloudSat, *Journal of Applied Meteorology and Climatology*, 55(9), 2063–2090,
1162 doi:10.1175/JAMC-D-15-0290.1.
- 1163 Hiley, M. J., M. S. Kulie, and R. Bennartz (2011), Uncertainty Analysis for CloudSat
1164 Snowfall Retrievals, *Journal of Applied Meteorology and Climatology*, 50(2), 399–418,
1165 doi:10.1175/2010JAMC2505.1.
- 1166 Hogan, R. J. (2007), A Variational Scheme for Retrieving Rainfall Rate and Hail Reflec-
1167 tivity Fraction from Polarization Radar, *Journal of Applied Meteorology and Climatol-*
1168 *ogy*, 46(10), 1544–1564, doi:10.1175/JAM2550.1.
- 1169 Hogan, R. J. (2008), Fast Lidar and Radar Multiple-Scattering Models. Part I: Small-
1170 Angle Scattering Using the Photon Variance–Covariance Method, *Journal of the At-*
1171 *mospheric Sciences*, 65(12), 3621–3635, doi:10.1175/2008JAS2642.1.
- 1172 Hogan, R. J. (2014), Fast Reverse-Mode Automatic Differentiation using Expression
1173 Templates in C++, *ACM Transactions on Mathematical Software*, 40(4), 1–16, doi:
1174 10.1145/2560359.
- 1175 Hogan, R. J. (2017), Adept 2.0: a combined automatic differentiation and array library for
1176 C++, doi:10.5281/ZENODO.1004730.
- 1177 Hogan, R. J., and A. J. Illingworth (1999), The Potential of Spaceborne Dual-
1178 Wavelength Radar to Make Global Measurements of Cirrus Clouds, *Journal*
1179 *of Atmospheric and Oceanic Technology*, 16(5), 518–531, doi:10.1175/1520-
1180 0426(1999)016<0518:TPOSDW>2.0.CO;2.
- 1181 Hogan, R. J., and C. D. Westbrook (2014), Equation for the Microwave Backscatter Cross
1182 Section of Aggregate Snowflakes Using the Self-Similar Rayleigh-Gans Approximation,
1183 *Journal of the Atmospheric Sciences*, 71(9), 3292–3301, doi:10.1175/JAS-D-13-0347.1.
- 1184 Hogan, R. J., P. N. Francis, H. Flentje, A. J. Illingworth, M. Quante, and J. Pelon (2003),
1185 Characteristics of mixed-phase clouds. I: Lidar, radar and aircraft observations from
1186 CLARE’98, *Quarterly Journal of the Royal Meteorological Society*, 129(592), 2089–
1187 2116, doi:10.1256/rj.01.208.

- 1188 Hogan, R. J., M. D. Behera, E. J. O'Connor, and A. J. Illingworth (2004), Estimate of the
1189 global distribution of stratiform supercooled liquid water clouds using the LITE lidar,
1190 *Geophysical Research Letters*, *31*(5), L05,106, doi:10.1029/2003GL018977.
- 1191 Hogan, R. J., L. Tian, P. R. A. Brown, C. D. Westbrook, A. J. Heymsfield, and J. D. East-
1192 ment (2012), Radar Scattering from Ice Aggregates Using the Horizontally Aligned
1193 Oblate Spheroid Approximation, *Journal of Applied Meteorology and Climatology*,
1194 *51*(3), 655–671, doi:10.1175/JAMC-D-11-074.1.
- 1195 Hogan, R. J., R. Honeyager, J. Tyynelä, and S. Kneifel (2017), Calculating the millimetre-
1196 wave scattering phase function of snowflakes using the self-similar Rayleigh-Gans Ap-
1197 proximation, *Quarterly Journal of the Royal Meteorological Society*, *143*(703), 834–844,
1198 doi:10.1002/qj.2968.
- 1199 Hou, A. Y., R. K. Kakar, S. Neeck, A. A. Azarbarzin, C. D. Kummerow, M. Kojima,
1200 R. Oki, K. Nakamura, and T. Iguchi (2014), The Global Precipitation Measure-
1201 ment Mission, *Bulletin of the American Meteorological Society*, *95*(5), 701–722, doi:
1202 10.1175/BAMS-D-13-00164.1.
- 1203 Illingworth, A. J., and T. M. Blackman (2002), The Need to Represent Raindrop Size
1204 Spectra as Normalized Gamma Distributions for the Interpretation of Polarization
1205 Radar Observations, *Journal of Applied Meteorology*, *41*(3), 286–297, doi:10.1175/1520-
1206 0450(2002)041<0286:TNTRRS>2.0.CO;2.
- 1207 Illingworth, A. J., R. J. Hogan, E. J. O'Connor, D. Bouniol, J. Delanoë, J. Pelon, A. Pro-
1208 tat, M. E. Brooks, N. Gaussiat, D. R. Wilson, D. P. Donovan, H. K. Baltink, G.-J. van
1209 Zadelhoff, J. D. Eastment, J. W. F. Goddard, C. L. Wrench, M. Haeffelin, O. A. Kras-
1210 nov, H. W. J. Russchenberg, J.-M. Piriou, F. Vinit, A. Seifert, A. M. Tompkins, and
1211 U. Willén (2007), Cloudnet, *Bulletin of the American Meteorological Society*, *88*(6),
1212 883–898, doi:10.1175/BAMS-88-6-883.
- 1213 Illingworth, A. J., H. W. Barker, A. Beljaars, M. Ceccaldi, H. Chepfer, N. Cler-
1214 baux, J. Cole, J. Delanoë, C. Domenech, D. P. Donovan, S. Fukuda, M. Hirakata,
1215 R. J. Hogan, A. Huenerbein, P. Kollias, T. Kubota, T. Nakajima, T. Y. Nakajima,
1216 T. Nishizawa, Y. Ohno, H. Okamoto, R. Oki, K. Sato, M. Satoh, M. W. Shephard,
1217 A. Velázquez-Blázquez, U. Wandinger, T. Wehr, and G.-J. van Zadelhoff (2015), The
1218 EarthCARE Satellite: The Next Step Forward in Global Measurements of Clouds,
1219 Aerosols, Precipitation, and Radiation, *Bulletin of the American Meteorological Society*,
1220 *96*(8), 1311–1332, doi:10.1175/BAMS-D-12-00227.1.

- 1221 Jiang, Z., M. Oue, J. Verlinde, E. E. Clothiaux, K. Aydin, G. Botta, and Y. Lu (2017),
1222 What Can We Conclude about the Real Aspect Ratios of Ice Particle Aggregates from
1223 Two-Dimensional Images?, *Journal of Applied Meteorology and Climatology*, *56*(3),
1224 725–734, doi:10.1175/JAMC-D-16-0248.1.
- 1225 Jullien, R. (1992), The application of fractals to colloidal aggregation, *Croatica Chemica*
1226 *Acta*, *65*(2), 215–235.
- 1227 Kalesse, H., W. Szyrmer, S. Kneifel, P. Kollias, and E. Luke (2016), Fingerprints of a
1228 riming event on cloud radar Doppler spectra: observations and modeling, *Atmospheric*
1229 *Chemistry and Physics*, *16*(5), 2997–3012, doi:10.5194/acp-16-2997-2016.
- 1230 Khvorostyanov, V. I., and J. A. Curry (2005), Fall Velocities of Hydrometeors in the At-
1231 mosphere: Refinements to a Continuous Analytical Power Law, *Journal of the Atmo-*
1232 *spheric Sciences*, *62*(12), 4343–4357, doi:10.1175/JAS3622.1.
- 1233 Kneifel, S., U. Löhnert, A. Battaglia, S. Crewell, and D. Siebler (2010), Snow scattering
1234 signals in ground-based passive microwave radiometer measurements, *Journal of Geo-*
1235 *physical Research*, *115*(D16), D16,214, doi:10.1029/2010JD013856.
- 1236 Kneifel, S., M. Maahn, G. Peters, and C. Simmer (2011), Observation of snowfall with
1237 a low-power FM-CW K-band radar (Micro Rain Radar), *Meteorology and Atmospheric*
1238 *Physics*, *113*(1-2), 75–87, doi:10.1007/s00703-011-0142-z.
- 1239 Kneifel, S., A. von Lerber, J. Tiira, D. Moisseev, P. Kollias, and J. Leinonen (2015),
1240 Observed relations between snowfall microphysics and triple-frequency radar mea-
1241 surements, *Journal of Geophysical Research: Atmospheres*, *120*(12), 6034–6055, doi:
1242 10.1002/2015JD023156.
- 1243 Kneifel, S., J. Dias Neto, D. Ori, D. Moisseev, J. Tyynelä, I. S. Adams, K.-S. Kuo,
1244 R. Bennartz, A. Berne, E. E. Clothiaux, P. Eriksson, A. J. Geer, R. Honeyager,
1245 J. Leinonen, and C. D. Westbrook (2018), Summer Snowfall Workshop: Scattering
1246 Properties of Realistic Frozen Hydrometeors from Simulations and Observations, as
1247 well as Defining a New Standard for Scattering Databases, *Bulletin of the American Me-*
1248 *teorological Society*, *99*(3), ES55–ES58, doi:10.1175/BAMS-D-17-0208.1.
- 1249 Kollias, P., S. Tanelli, A. Battaglia, and A. Tatarevic (2014), Evaluation of EarthCARE
1250 Cloud Profiling Radar Doppler Velocity Measurements in Particle Sedimentation
1251 Regimes, *Journal of Atmospheric and Oceanic Technology*, *31*(2), 366–386, doi:
1252 10.1175/JTECH-D-11-00202.1.

Confidential manuscript submitted to *JGR-Atmospheres*

- 1253 Kulie, M. S., and R. Bennartz (2009), Utilizing Spaceborne Radars to Retrieve Dry
1254 Snowfall, *Journal of Applied Meteorology and Climatology*, 48(12), 2564–2580, doi:
1255 10.1175/2009JAMC2193.1.
- 1256 Kulie, M. S., L. Milani, N. B. Wood, S. A. Tushaus, R. Bennartz, and T. S. L'Ecuyer
1257 (2016), A Shallow Cumuliform Snowfall Census Using Spaceborne Radar, *Journal of*
1258 *Hydrometeorology*, 17(4), 1261–1279, doi:10.1175/JHM-D-15-0123.1.
- 1259 Langleben, M. P. (1954), The terminal velocity of snowflakes, *Quarterly Journal of the*
1260 *Royal Meteorological Society*, 80(344), 174–181, doi:10.1002/qj.49708034404.
- 1261 Leinonen, J., and D. Moisseev (2015), What do triple-frequency radar signatures reveal
1262 about aggregate snowflakes?, *Journal of Geophysical Research: Atmospheres*, 120(1),
1263 229–239, doi:10.1002/2014JD022072.
- 1264 Leinonen, J., and W. Szyrmer (2015), Radar signatures of snowflake riming: A modeling
1265 study, *Earth and Space Science*, 2(8), 346–358, doi:10.1002/2015EA000102.
- 1266 Leinonen, J., M. D. Lebsock, G. L. Stephens, and K. Suzuki (2016), Improved Retrieval
1267 of Cloud Liquid Water from CloudSat and MODIS, *Journal of Applied Meteorology and*
1268 *Climatology*, 55(8), 1831–1844, doi:10.1175/JAMC-D-16-0077.1.
- 1269 Li, H., D. Moisseev, and A. von Lerber (2018), How Does Riming Affect Dual-
1270 Polarization Radar Observations and Snowflake Shape?, *Journal of Geophysical Re-*
1271 *search: Atmospheres*, 123(11), 6070–6081, doi:10.1029/2017JD028186.
- 1272 Liebe, H. J. (1985), An updated model for millimeter wave propagation in moist air, *Ra-*
1273 *dio Science*, 20(5), 1069–1089.
- 1274 Lin, Y., and B. A. Colle (2011), A New Bulk Microphysical Scheme That Includes Rim-
1275 ing Intensity and Temperature-Dependent Ice Characteristics, *Monthly Weather Review*,
1276 139(3), 1013–1035, doi:10.1175/2010MWR3293.1.
- 1277 Lin, Y., L. J. Donner, and B. A. Colle (2011), Parameterization of Riming Intensity and
1278 Its Impact on Ice Fall Speed Using ARM Data, *Monthly Weather Review*, 139(3), 1036–
1279 1047, doi:10.1175/2010MWR3299.1.
- 1280 Liu, G. (2008), Deriving snow cloud characteristics from CloudSat observations, *Journal*
1281 *of Geophysical Research*, 113(D8), D00A09, doi:10.1029/2007JD009766.
- 1282 Löhnert, U., S. Kneifel, A. Battaglia, M. Hagen, L. Hirsch, and S. Crewell (2011), A
1283 Multisensor Approach Toward a Better Understanding of Snowfall Microphysics: The
1284 TOSCA Project, *Bulletin of the American Meteorological Society*, 92(5), 613–628, doi:
1285 10.1175/2010BAMS2909.1.

- 1286 Maahn, M., and U. Löhnert (2017), Potential of Higher-Order Moments and Slopes of
1287 the Radar Doppler Spectrum for Retrieving Microphysical and Kinematic Properties of
1288 Arctic Ice Clouds, *Journal of Applied Meteorology and Climatology*, 56(2), 263–282,
1289 doi:10.1175/JAMC-D-16-0020.1.
- 1290 Maahn, M., U. Löhnert, P. Kollias, R. C. Jackson, and G. M. McFarquhar (2015), De-
1291 veloping and Evaluating Ice Cloud Parameterizations for Forward Modeling of Radar
1292 Moments Using in situ Aircraft Observations, *Journal of Atmospheric and Oceanic Tech-*
1293 *nology*, 32(5), 880–903, doi:10.1175/JTECH-D-14-00112.1.
- 1294 Mace, G., and S. Benson (2017), Diagnosing Cloud Microphysical Process Information
1295 from Remote Sensing Measurements—A Feasibility Study Using Aircraft Data. Part I:
1296 Tropical Anvils Measured during TC4, *Journal of Applied Meteorology and Climatology*,
1297 56(3), 633–649, doi:10.1175/JAMC-D-16-0083.1.
- 1298 Mason, S. L., J. C. Chiu, R. J. Hogan, and L. Tian (2017), Improved rain-rate and drop-
1299 size retrievals from airborne and spaceborne Doppler radar, *Atmospheric Chemistry and*
1300 *Physics Discussions*, pp. 1–34, doi:10.5194/acp-2017-280.
- 1301 Mitchell, D. (1996), Use of mass-and area-dimensional power laws for determining precip-
1302 itation particle terminal velocities, *Journal of the atmospheric sciences*.
- 1303 Mitchell, D. L., and A. J. Heymsfield (2005), Refinements in the Treatment of Ice Parti-
1304 cle Terminal Velocities, Highlighting Aggregates, *Journal of the Atmospheric Sciences*,
1305 62(5), 1637–1644, doi:10.1175/JAS3413.1.
- 1306 Mitchell, D. L., R. Zhang, and R. L. Pitter (1990), Mass-Dimensional Relationships for
1307 Ice Particles and the Influence of Riming on Snowfall Rates, *Journal of Applied Meteo-*
1308 *rology*, 29(2), 153–163, doi:10.1175/1520-0450(1990)029<0153:MDRFIP>2.0.CO;2.
- 1309 Moisseev, D., A. von Lerber, and J. Tiira (2017), Quantifying the effect of riming on
1310 snowfall using ground-based observations, *Journal of Geophysical Research: Atmo-*
1311 *spheres*, 122, doi:10.1002/2016JD026272.
- 1312 Morrison, H., and J. A. Milbrandt (2015), Parameterization of Cloud Microphysics Based
1313 on the Prediction of Bulk Ice Particle Properties. Part I: Scheme Description and Ideal-
1314 ized Tests, *Journal of the Atmospheric Sciences*, 72(1), 287–311, doi:10.1175/JAS-D-14-
1315 0065.1.
- 1316 Morrison, H., J. A. Milbrandt, G. H. Bryan, K. Ikeda, S. A. Tessendorf, and G. Thomp-
1317 son (2015), Parameterization of Cloud Microphysics Based on the Prediction of Bulk
1318 Ice Particle Properties. Part II: Case Study Comparisons with Observations and Other

- 1319 Schemes, *Journal of the Atmospheric Sciences*, 72(1), 312–339, doi:10.1175/JAS-D-14-
1320 0066.1.
- 1321 Mosimann, L. (1995), An improved method for determining the degree of snow crys-
1322 tal riming by vertical Doppler radar, *Atmospheric Research*, 37(4), 305–323, doi:
1323 10.1016/0169-8095(94)00050-N.
- 1324 National Academies of Sciences Engineering and Medicine (2018), *Thriving on Our*
1325 *Changing Planet: A Decadal Strategy for Earth Observation from Space*, National
1326 Academies Press, Washington, D.C., doi:10.17226/24938.
- 1327 Newman, A. J., P. A. Kucera, and L. F. Bliven (2009), Presenting the Snowflake Video
1328 Imager (SVI), *Journal of Atmospheric and Oceanic Technology*, 26(2), 167–179, doi:
1329 10.1175/2008JTECHA1148.1.
- 1330 Palerme, C., J. E. Kay, C. Genthon, T. L'Ecuyer, N. B. Wood, and C. Claud (2014), How
1331 much snow falls on the Antarctic ice sheet?, *The Cryosphere*, 8(4), 1577–1587, doi:
1332 10.5194/tc-8-1577-2014.
- 1333 Petäjä, T., E. J. O'Connor, D. Moisseev, V. A. Sinclair, A. J. Manninen, R. Väänänen,
1334 A. von Lerber, J. A. Thornton, K. Nicoll, W. Petersen, V. Chandrasekar, J. N. Smith,
1335 P. M. Winkler, O. Krüger, H. Hakola, H. Timonen, D. Brus, T. Laurila, E. Asmi, M.-
1336 L. Riekkola, L. Mona, P. Massoli, R. Engelmann, M. Komppula, J. Wang, C. Kuang,
1337 J. Bäck, A. Virtanen, J. Levula, M. Ritsche, and N. Hickmon (2016), BAECC: A Field
1338 Campaign to Elucidate the Impact of Biogenic Aerosols on Clouds and Climate, *Bul-*
1339 *letin of the American Meteorological Society*, 97(10), 1909–1928, doi:10.1175/BAMS-D-
1340 14-00199.1.
- 1341 Rodgers, C. D. (2000), *Inverse methods for atmospheric sounding: theory and practice*,
1342 World Scientific, Singapore.
- 1343 Schmitt, C. G., and A. J. Heymsfield (2010), The Dimensional Characteristics of Ice Crys-
1344 tal Aggregates from Fractal Geometry, *Journal of the Atmospheric Sciences*, 67(5),
1345 1605–1616, doi:10.1175/2009JAS3187.1.
- 1346 Shupe, M. D., P. Kollias, S. Y. Matrosov, and T. L. Schneider (2004), Deriv-
1347 ing Mixed-Phase Cloud Properties from Doppler Radar Spectra, *Journal of*
1348 *Atmospheric and Oceanic Technology*, 21(4), 660–670, doi:10.1175/1520-
1349 0426(2004)021<0660:DMCPFD>2.0.CO;2.
- 1350 Stein, T. H. M., C. D. Westbrook, and J. C. Nicol (2015), Fractal geometry of aggregate
1351 snowflakes revealed by triple-wavelength radar measurements, *Geophysical Research*

- 1352 *Letters*, 42(1), 176–183, doi:10.1002/2014GL062170.
- 1353 Stephens, G. L., D. G. Vane, R. J. Boain, G. G. Mace, K. Sassen, Z. Wang, A. J. Illing-
1354 worth, E. J. O'Connor, W. B. Rossow, S. L. Durden, and others (2002), The CloudSat
1355 mission and the A-Train: A new dimension of space-based observations of clouds and
1356 precipitation, *Bulletin of the American Meteorological Society*, 83(12), 1771–1790.
- 1357 Szyrmer, W., and I. Zawadzki (2014a), Snow Studies. Part III: Theoretical Derivations for
1358 the Ensemble Retrieval of Snow Microphysics from Dual-Wavelength Vertically Point-
1359 ing Radars, *Journal of the Atmospheric Sciences*, 71(3), 1158–1170, doi:10.1175/JAS-D-
1360 12-0285.1.
- 1361 Szyrmer, W., and I. Zawadzki (2014b), Snow Studies. Part IV: Ensemble Retrieval of
1362 Snow Microphysics from Dual-Wavelength Vertically Pointing Radars, *Journal of the*
1363 *Atmospheric Sciences*, 71(3), 1171–1186, doi:10.1175/JAS-D-12-0286.1.
- 1364 Tan, I., T. Storelvmo, and M. D. M. Zelinka (2016), Observational constraints on mixed-
1365 phase clouds imply higher climate sensitivity, *Science*, 352(6282), 224–227, doi:
1366 10.1126/science.aad5300.
- 1367 Tanelli, S., S. L. Durden, E. Im, G. M. Heymsfield, P. Racette, and D. O. Starr (2009),
1368 Next-generation spaceborne Cloud Profiling Radars, in *2009 IEEE Radar Conference*,
1369 pp. 1–4, IEEE, doi:10.1109/RADAR.2009.4977116.
- 1370 Testud, J., S. Oury, R. A. Black, P. Amayenc, and X. Dou (2001), The Concept of
1371 “Normalized” Distribution to Describe Raindrop Spectra: A Tool for Cloud
1372 Physics and Cloud Remote Sensing, *Journal of Applied Meteorology*, 40(6), 1118–1140,
1373 doi:10.1175/1520-0450(2001)040<1118:TCOND>2.0.CO;2.
- 1374 Tiira, J., D. N. Moisseev, A. von Lerber, D. Ori, A. Tokay, L. F. Bliven, and W. Petersen
1375 (2016), Ensemble mean density and its connection to other microphysical properties of
1376 falling snow as observed in Southern Finland, *Atmospheric Measurement Techniques*,
1377 9(9), 4825–4841, doi:10.5194/amt-9-4825-2016.
- 1378 Twomey, S. (1977), *Introduction to the Mathematics of Inversion in Remote Sensing and*
1379 *Indirect*, Elsevier Scientific Publishing.
- 1380 von Lerber, A., D. Moisseev, L. F. Bliven, W. Petersen, A.-M. Harri, and V. Chandrasekar
1381 (2017), Microphysical Properties of Snow and Their Link to Ze-S Relations during
1382 BAECC 2014, *Journal of Applied Meteorology and Climatology*, 56(6), 1561–1582, doi:
1383 10.1175/JAMC-D-16-0379.1.

Confidential manuscript submitted to *JGR-Atmospheres*

- 1384 Westbrook, C. D., R. C. Ball, P. R. Field, and A. J. Heymsfield (2004), Theory of growth
1385 by differential sedimentation, with application to snowflake formation, *Physical Review*
1386 *E*, 70(2), 021,403, doi:10.1103/PhysRevE.70.021403.
- 1387 Yin, M., G. Liu, R. Honeyager, and F. Joseph Turk (2017), Observed differences of
1388 triple-frequency radar signatures between snowflakes in stratiform and convective
1389 clouds, *Journal of Quantitative Spectroscopy and Radiative Transfer*, 193, 13–20, doi:
1390 10.1016/J.JQSRT.2017.02.017.
- 1391 Zikmunda, J., and G. Vali (1972), Fall Patterns and Fall Velocities of Rimed Ice Crys-
1392 tals, *Journal of the Atmospheric Sciences*, 29(7), 1334–1347, doi:10.1175/1520-
1393 0469(1972)029<1334:FPAFVO>2.0.CO;2.

Figure 1.

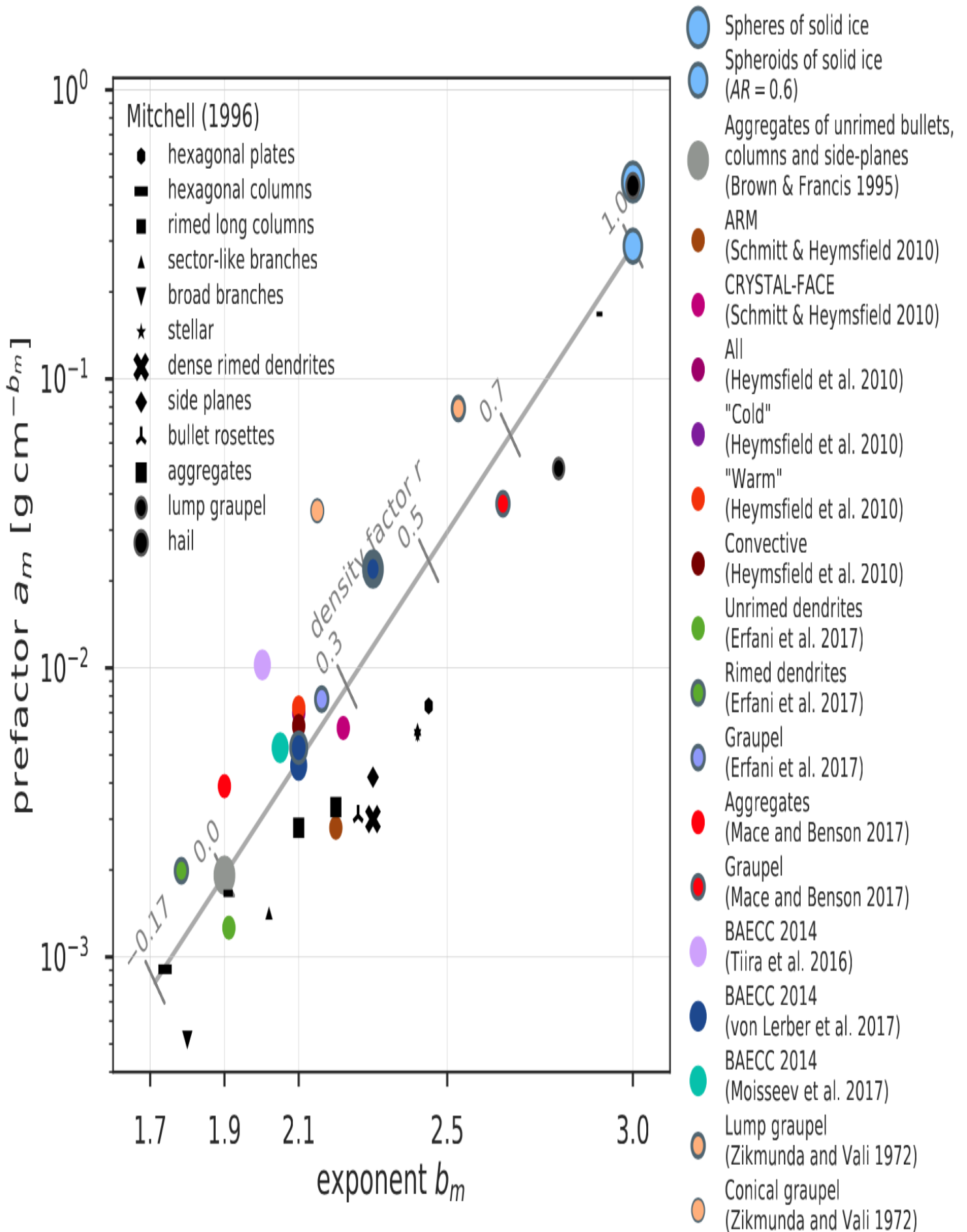


Figure 2.

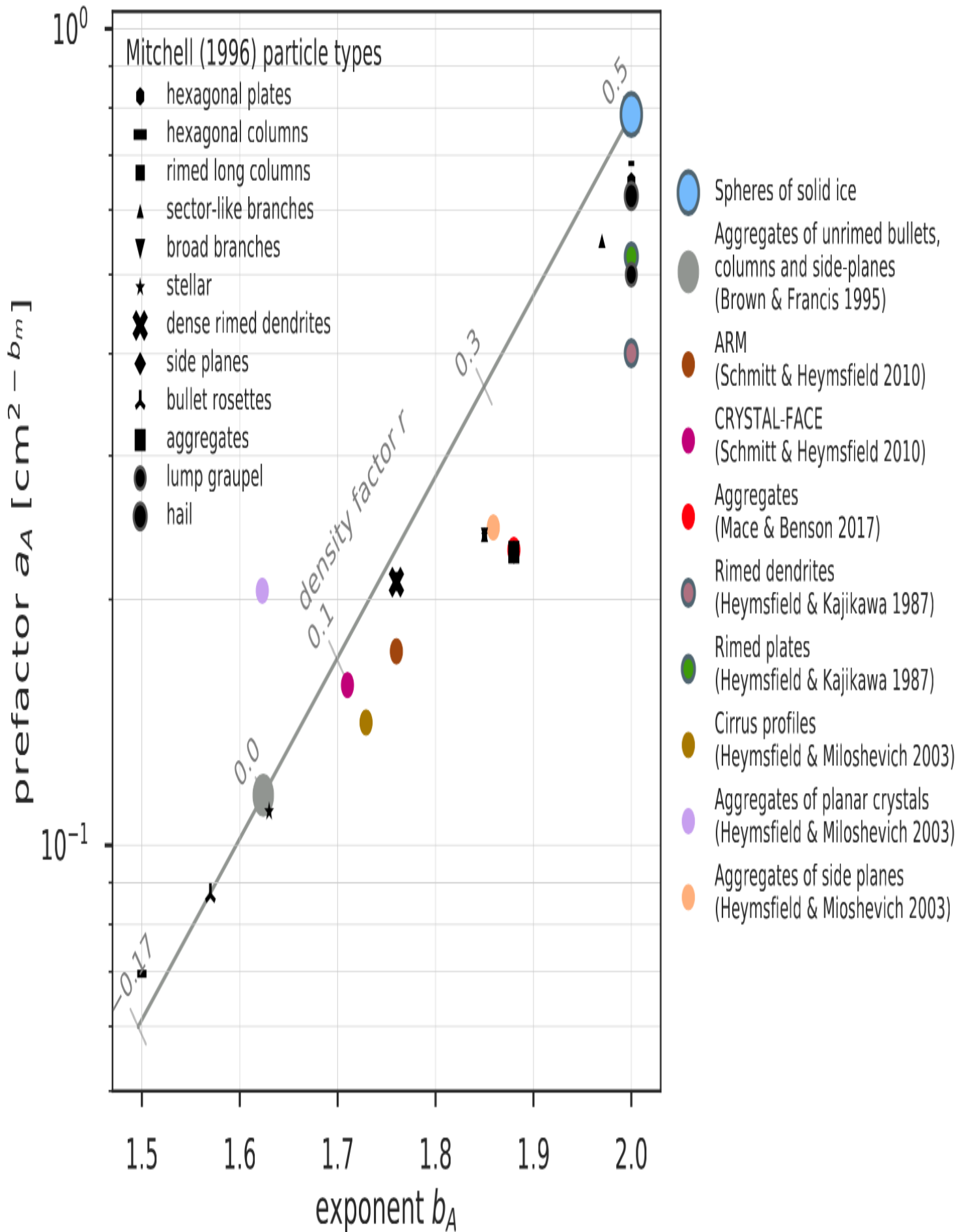


Figure 3.

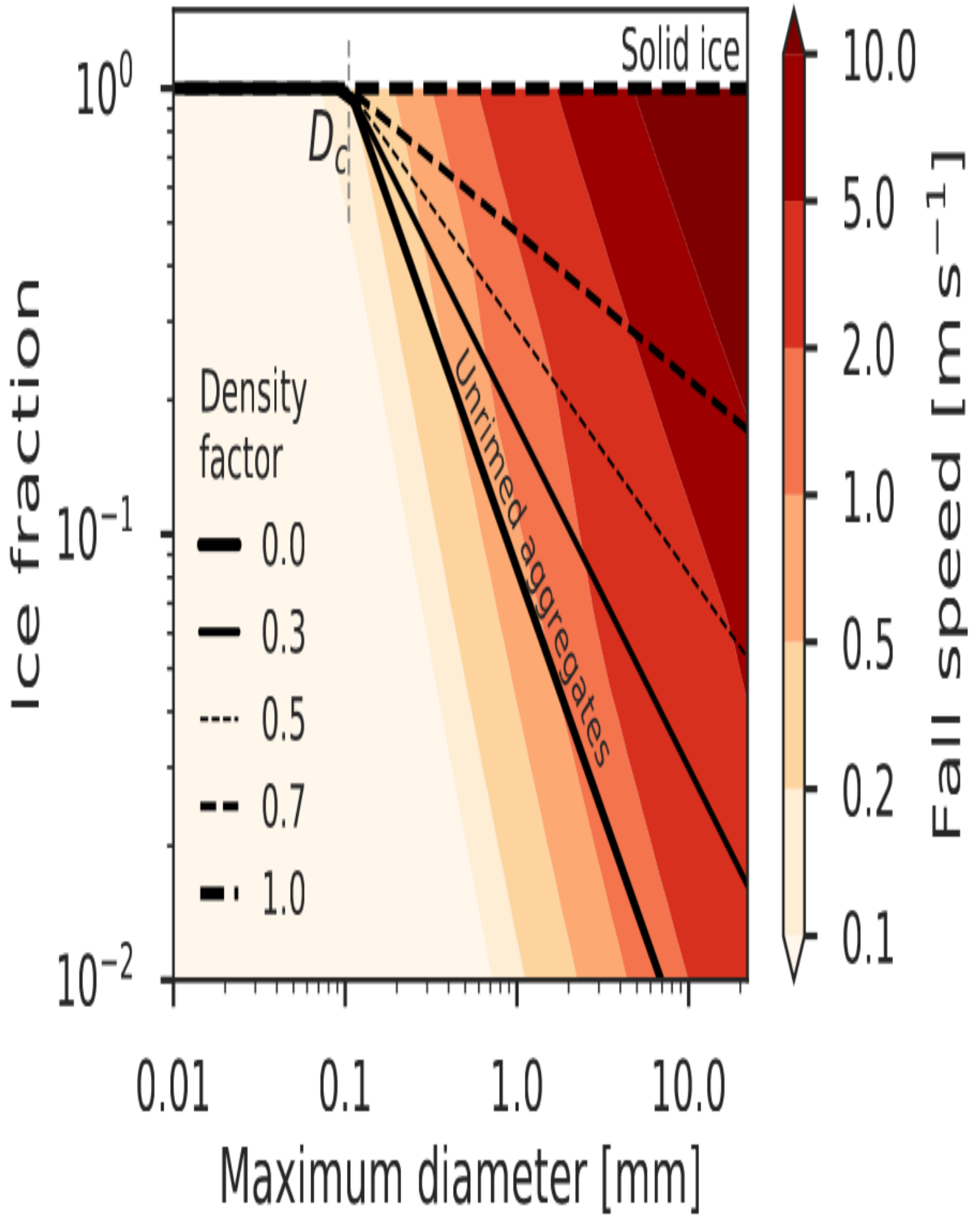


Figure 4.

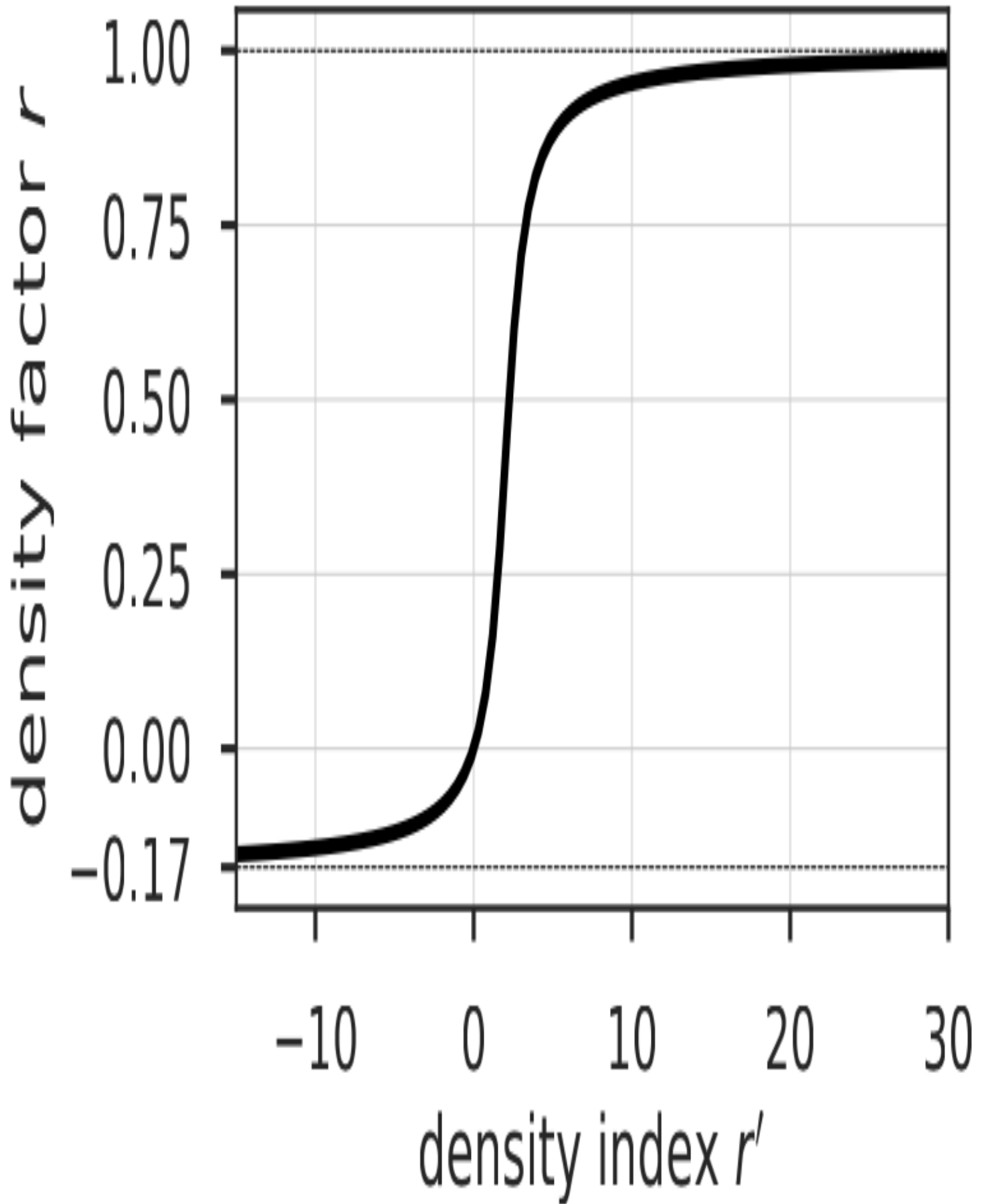


Figure 5.

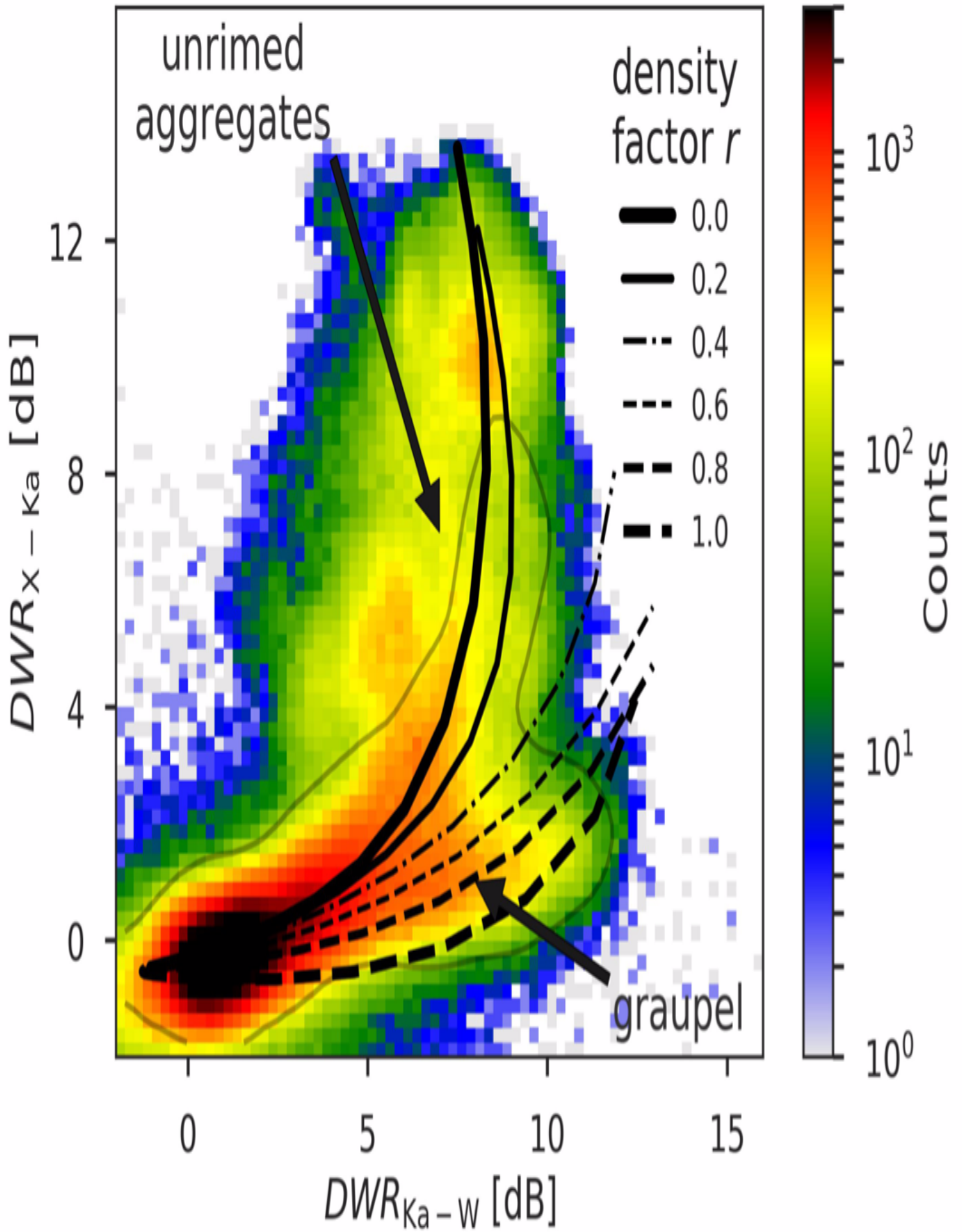


Figure 6.

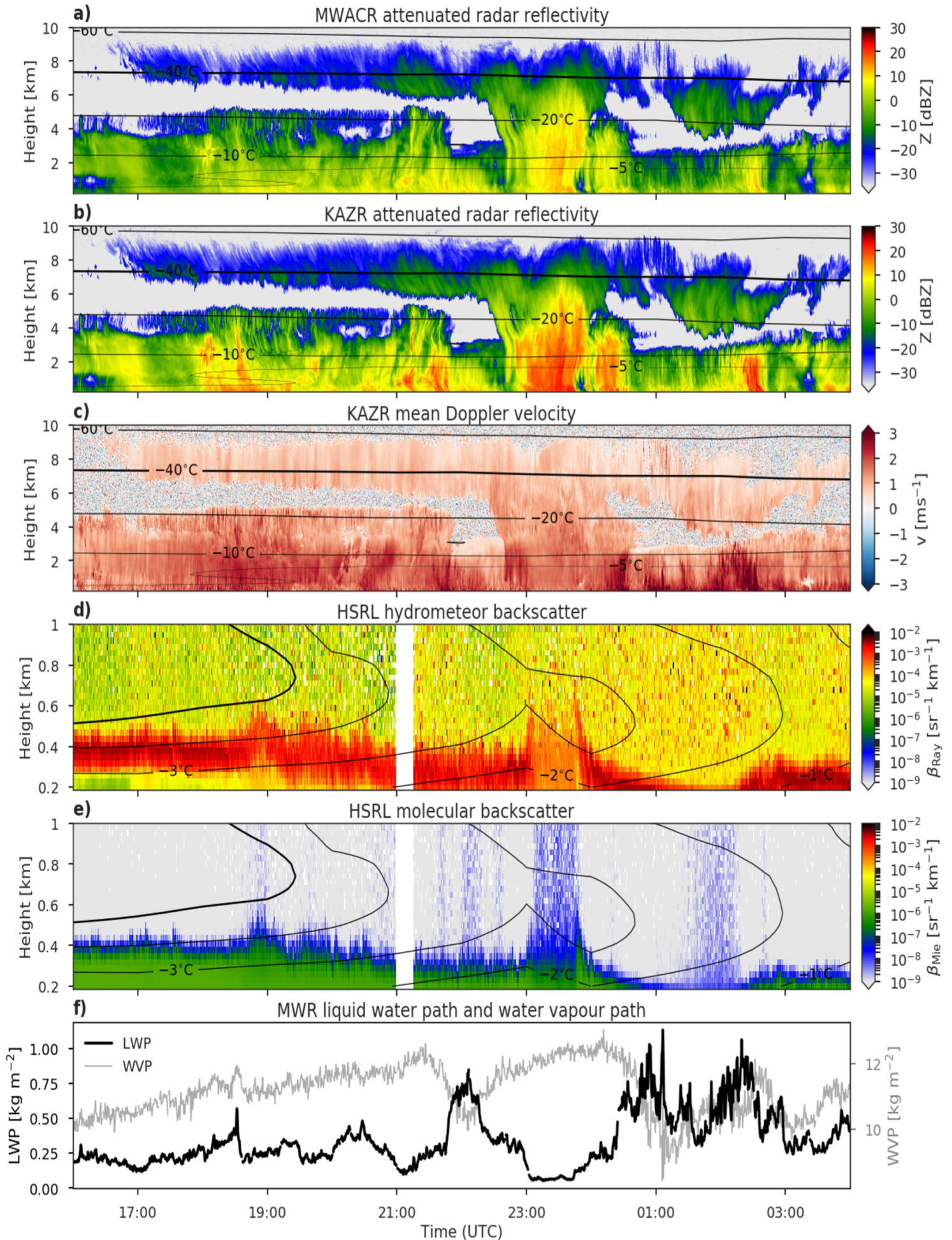


Figure 7.

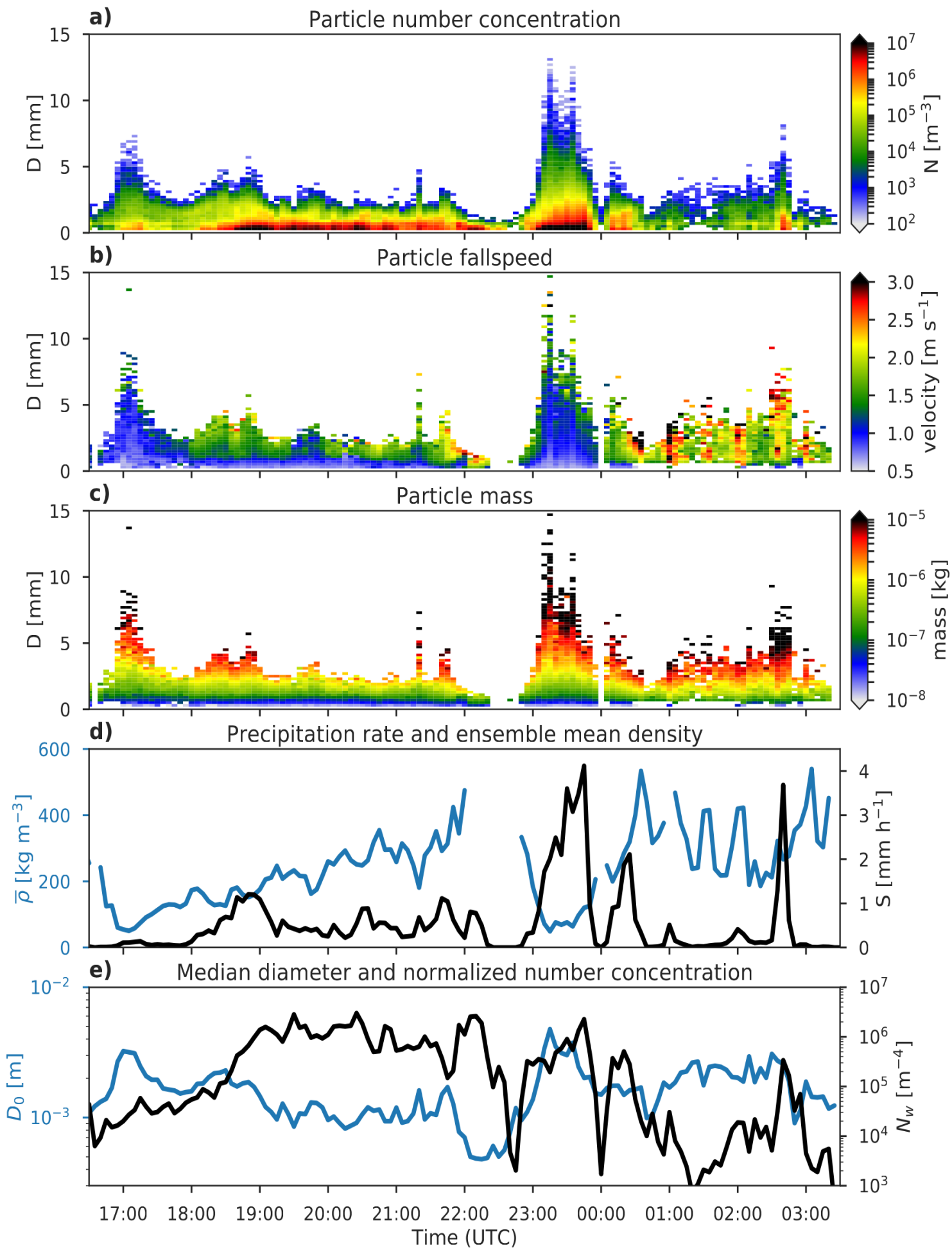


Figure 8.

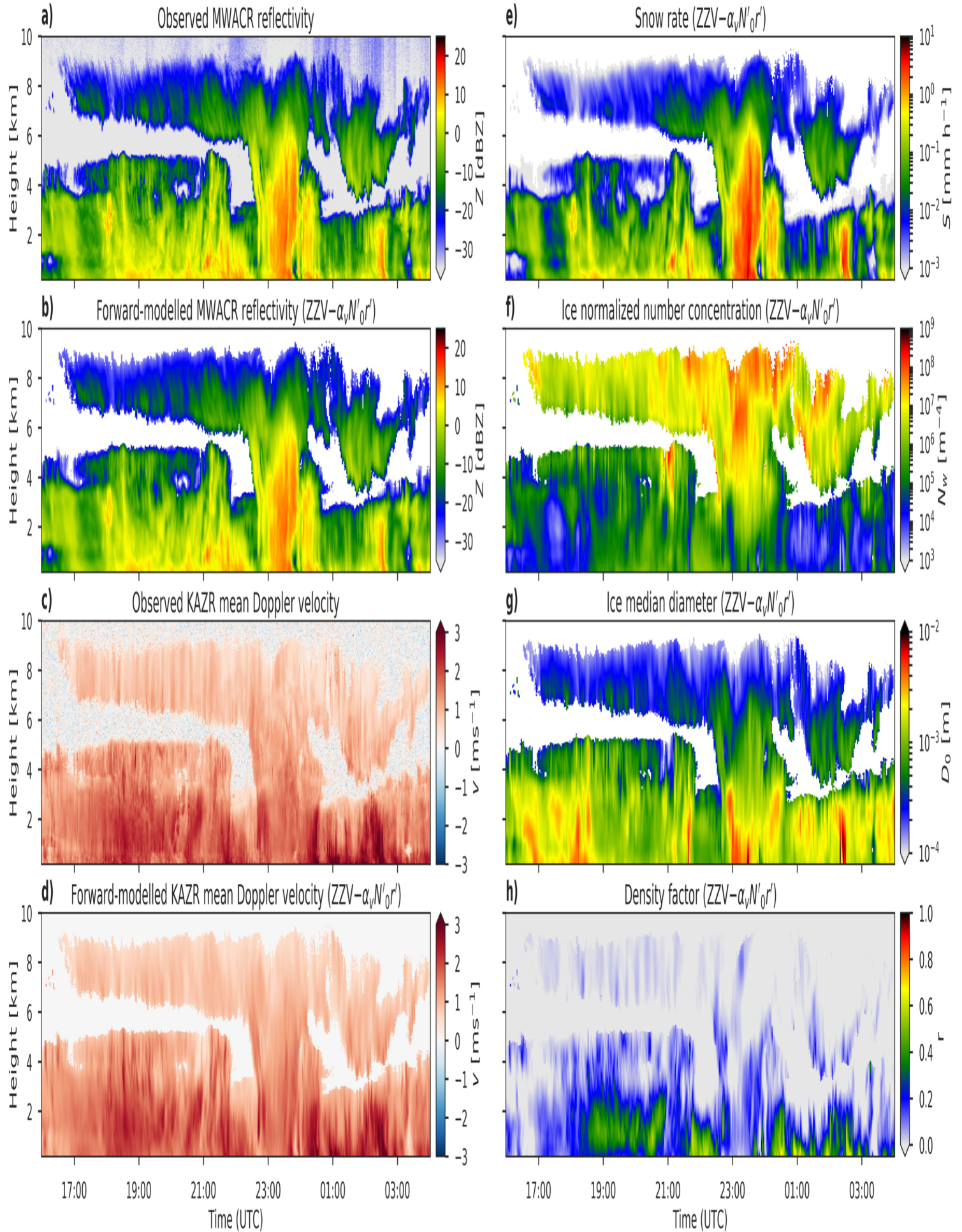


Figure 9.

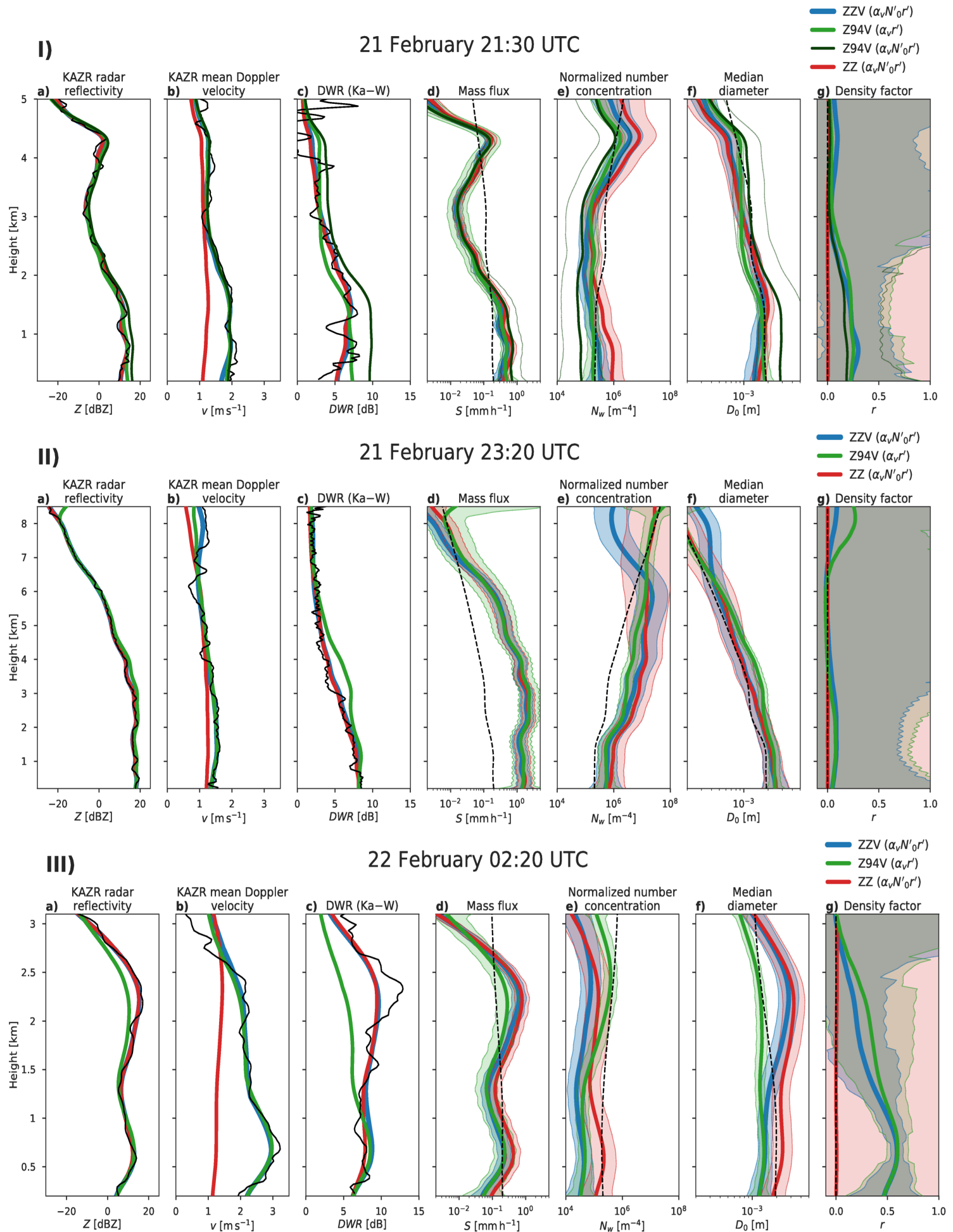


Figure 10.

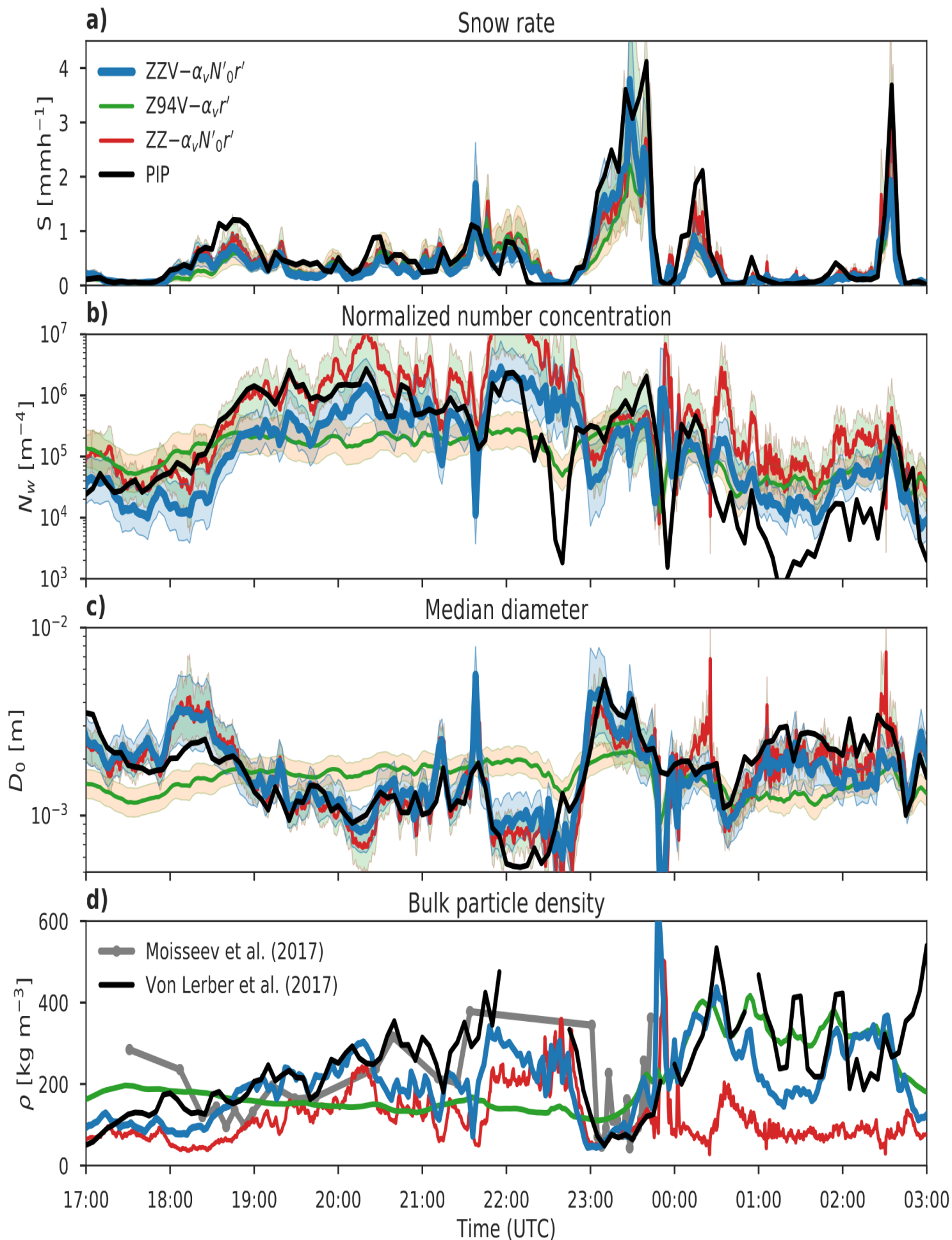


Figure 11.

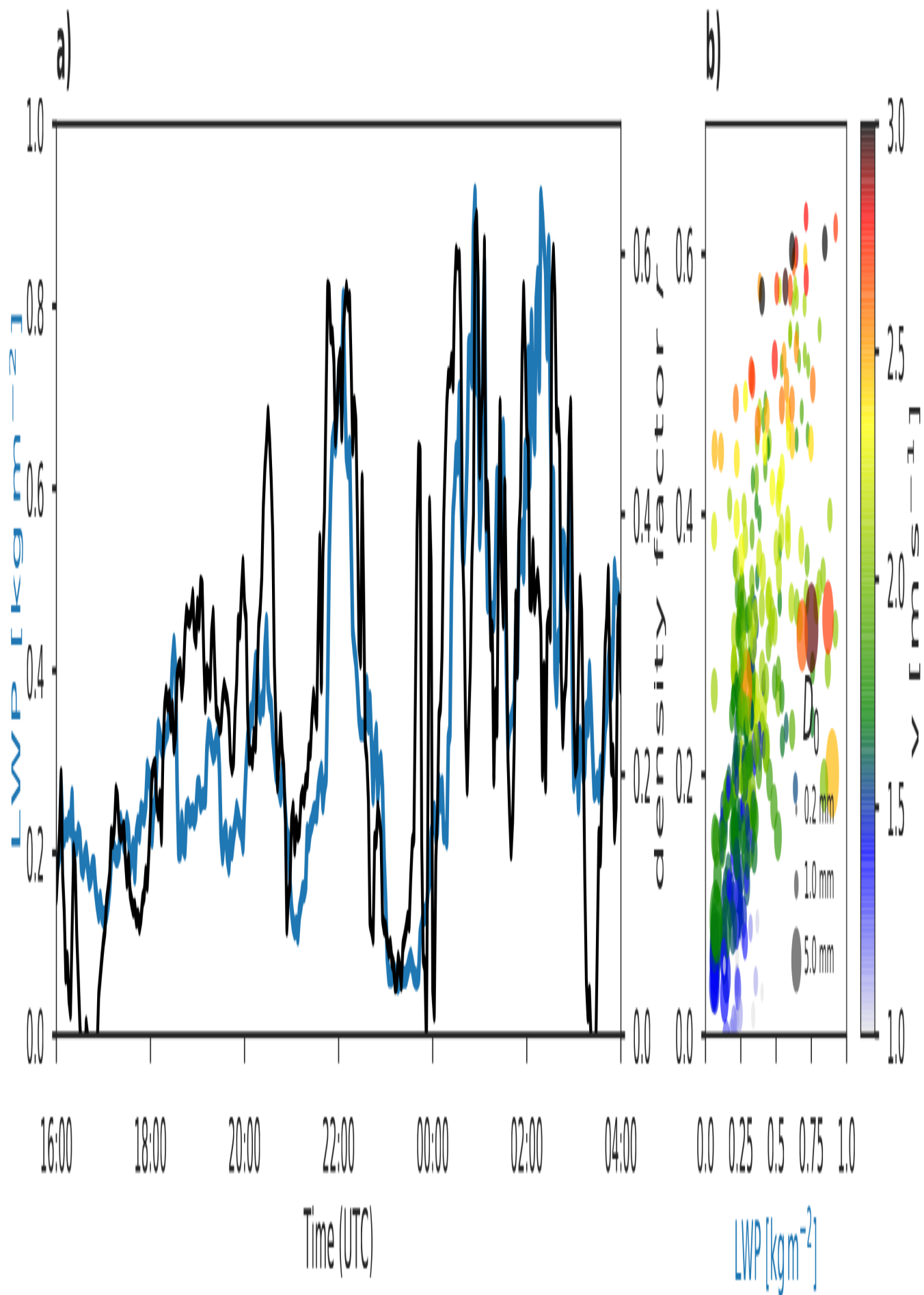


Figure 12.

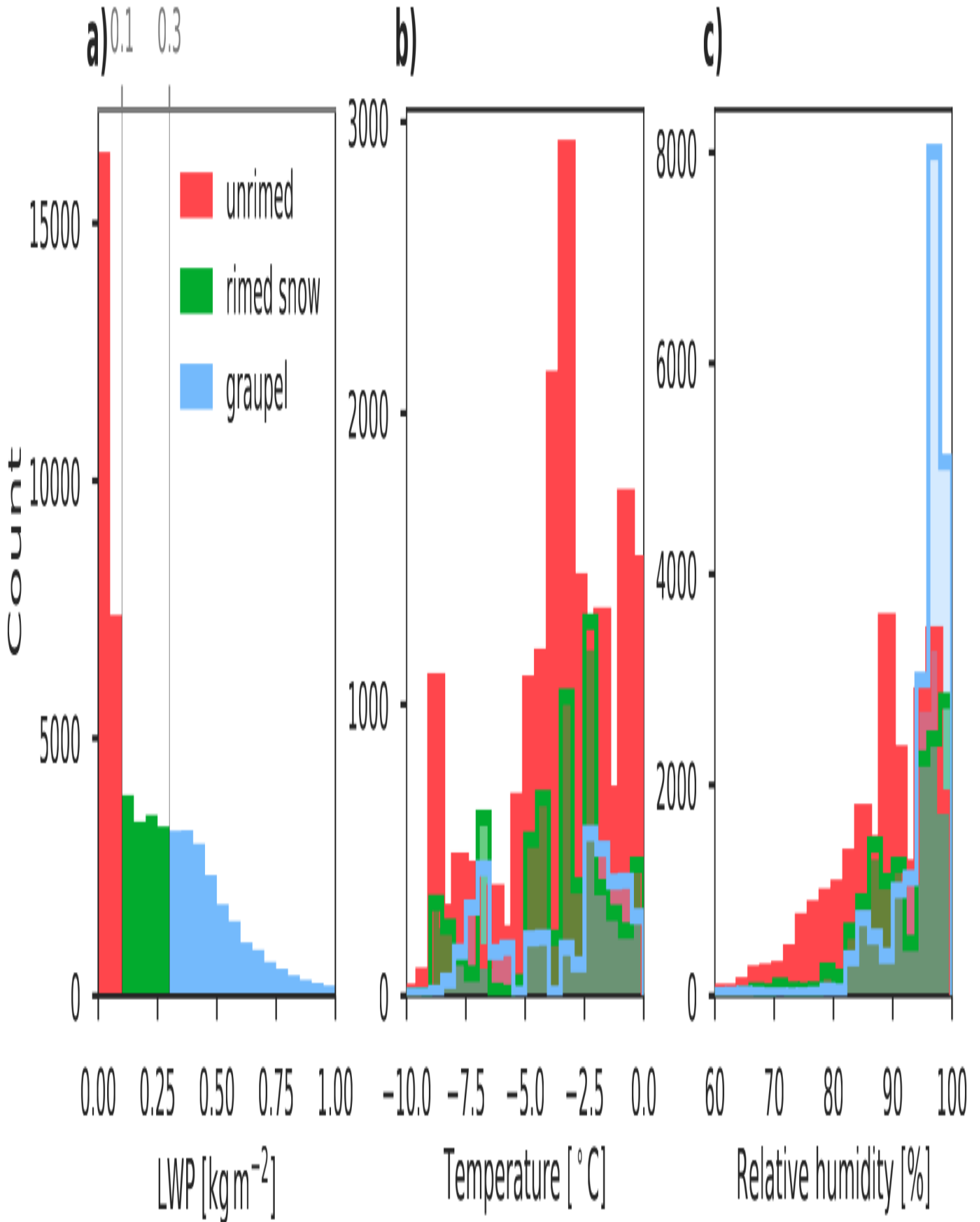


Figure 13.

